INVESTIGATION OF STRAIN ELASTOGRAPHY TO ASSESS BENIGN AND MALIGNANT TUMORS

A Thesis

by

XINYI GOU

Submitted to the Graduate and Professional School of
Texas A&M University
in partial fulfillment of the requirements for the degree of

MASTER OF SCIENCE

Chair of Committee,	Raffaella Righetti
Committee Members,	Junuthula N. Reddy
	Jun Zou
	Xiaoning Qian
Head of Department,	Miroslav M. Begovic

December 2021

Major Subject: Electrical Engineering

ABSTRACT

Poroelastography is a new subfield of ultrasound elastography that enables cost-effective and non-invasive imaging of mechanical properties of tissues. Assessment of changes in the mechanical properties of tumors is of great clinical significance as the onset of pathology often triggers these changes. Interstitial fluid pressure (IFP) and Solid stress (SS) are clinically significant tumor parameters in cancer initiation, growth, and metastasis. Although IFP and SS are crucial parameters for cancer prognosis and treatments, there are currently no non-invasive methods to assess this parameter in vivo. The use of poroelastography to noninvasively assess IFP and SS in cancers has not been thoroughly investigated yet. In this thesis, we used a novel Finite element modeling (FEM) technique to examine the effect of IFP and SS on elastographic strains generated inside a tumor model in a poroelastography experiment, including fundamental strains (normal and shear strains) and derived strains (principal and Von Mises strains). A variety of simulated phantoms with different properties of backgrounds and inclusions are simulated. We proposed the first principal and the Von Mises strain as sensitive elastographic markers associated with IFP and SS changes in simulated cancers. Our simulation results show that SS causes shear strains inside the tumor and leads to spatial variations in derived strains, while IFP causes uniformly reduction in derived strains. Using ultrasound simulations, we demonstrated that the observations from the FE study are also applicable with noisy experimental conditions except for the radial shear strain and the second principal strain. Additionally, as a proof of concept, this study used previously obtained mice data to demonstrate the feasibility of imaging Von Mises strains in vivo. This study may help understand the effect of IFP and SS on the strains generated in a tumor during a poroelastography experiment and may also result in new methods to check for IFP and SS in cancers in vivo.

DEDICATION

To my family and friends. Thank you for your love and caring. Special thanks to my amazing mother, who is proud of me, for her countless sacrifices to raise me up and to give me the best possible education. I love you and I couldn't have made it this far without you.

ACKNOWLEDGMENTS

I would like to express my deep and sincere gratitude to my advisor, Dr. Righetti, for offering me the golden opportunity to work on this interesting research and providing me the invaluable advice throughout this research. Thank you, Dr. Righetti, for always taking the time to check on me and see how I am doing. Whenever I'm facing challenges, you are always come to my aid. I don't know what I would do without someone so good to me like you. Without your support and constant feedback, I would not have completed my second Master and survived my life's lowest point.

I would also like to thank Dr. Tauhidul Islam, Dr. Songyuan Tang, Dr. Sharmin Majumder, and Dr. Hadiur Rahman Khan. They have provided me with extensive professional guidance throughout my studies. They are experts in Abaqus modeling and strain analysis. They always patiently helped me out when I am stuck. I am extremely grateful for what they have offered me.

CONTRIBUTORS AND FUNDING SOURCES

Contributors

This work was supported by a thesis committee consisting of Professor Raffaella Righetti, Professor Jun Zou, and Professor Xiaoning Qian of the Department of Electrical Engineering and Professor Junuthula N. Reddy of the Department of Mechanical Engineering.

The ultrasound simulation and in-vivo data for Chapter 4 were pre-processed by Dr. Sharmin Majumder and Dr. Hadiur Rahman Khan of the Department of Electrical Engineering using previously developed DPHS model in our lab.

All other work conducted for the thesis was completed by the student independently.

Funding Sources

There are no outside funding contributions to acknowledge related to the research and compilation of this document.

NOMENCLATURE

FEM	Finite Element Method
IFP	Interstitial Fluid Pressure
SS	Solid Stress

TABLE OF CONTENTS

LIST OF FIGURES

FIGURE Page

LIST OF TABLES

TABLE Page

1. INTRODUCTION

1.1 Background

1.1.1 The Breast Anatomy and Breast Cancer

Cancer is still the leading cause of mortality in the United States, according to the CDC's 2020 Annual report [1]. The most common type of female cancer is breast cancer. Breast cancer is a prevalent disease that affects many families, and many patients diagnosed with invasive cancer face the possibility of mastectomy surgery or death. In the United States, approximately 255,000 females and 2300 males are diagnosed with breast cancer every year [2]. According to the American Cancer Society, invasive breast cancer affects one in every eight women at some point in their lives, and it kills one out of every thirty-nine women from the disease [3].

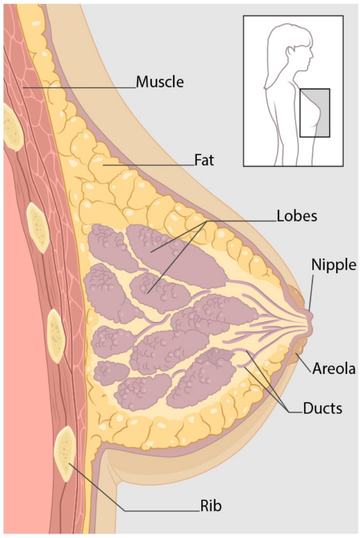

Figure 1.1: Cross section view of the breast from CDC [2]

Normal breasts are composed of fatty tissue, connective tissue, breast tissue, numerous blood vessels, nerves, and lymphatic vessels. The structure of female breasts mainly contains lobules, ducts, and connective tissue, as shown in Fig. 1.1. Lobules are glands that produce milk, which is transported to the nipple via the ducts. The whole breast is held together by connective tissue, which is composed of fibrous and fatty tissue. Cancer can occur in most tissues in the breast, including milk ducts (called ductal carcinomas), breast glands or breast lobules (called breast lobular carcinomas), and fat or connective tissues (called sarcomas). Ductal carcinoma and breast lobular carcinomas account for most breast cancers [2].

Early-stage breast cancer usually presents with no symptoms. Breast cancer is often detected by the discovery of a lump that is noticeably firmer than the surrounding breast tissue. Patients usually palpate the mass by themselves. The mass frequently indicates pathology if one breast develops a firm, distinct thickening but the other does not. There is no adhesion between early cancer and the skin, and therefore the mass can be pushed freely beneath the skin with the fingertips. Eventually, the lump develops and adheres to the chest wall or skin. At this point, patients can not push or separate the lump from the surrounding skin. The lump may be painful, but the pain is not a reliable symptom because cancer seldom causes pain. The lymph nodes, particularly those in the affected armpit, may feel like small hard bumps if cancer has migrated and may encrust to the chest wall or skin. The process is usually painless or just somewhat uncomfortable. The first signs and symptoms of cancer may not show up until it has spread to other organs. For example, coughing or trouble breathing are signs that appear after cancer has spread to the lungs. The estimated survival rate of cancer highly depends on the severeness of the breast tumor. Despite some progress in addressing breast cancer, more analysis is needed to improve disparities in cancer screening.

1.1.2 Current Breast Examination Technology

There are currently a considerable number of methods to detect breast cancers. Biopsies are commonly utilized to collect tissue samples and histologically diagnose tumors. Mammography and ultrasound scans are frequently used to detect and classify breast cancers noninvasively, but there are certain drawbacks associated with the use of the two methods. Mammography has a high rate of false-negative results, especially for patients with dense tissue, while conventional ultrasound imaging has poor specificity and sensitivity in lesion classification that can result in redundant procedures and detection failure [4]. The elastography should never be performed or interpreted in isolation, always in conjunction with B-mode or morphological features.

Lesion classification can be enhanced through the use of ultrasound elastography, which is a method to complement ultrasound scans [5]. In practice, ultrasound elastography is never conducted or interpreted in isolation, always in conjunction with B-mode or morphological characteristics. The key strengths of using ultrasound elastography are that the method is inexpensive, non-invasive, and uncomplicated. It makes up for the shortcomings of conventional ultrasound and enriches the disease's diagnosis information and diagnosis methods. This method has a particular clinical guiding significance for the choice of cancer treatment and has an excellent clinical application prospect.

1.1.3 Tumor Classifications

Tumors are lumps or abnormal growth of tissues in the human body that may be divided into two general categories: benign (noncancerous) and malignant (cancerous) tumors. Benign tumors are not as harmful as malignant tumors because they are not likely to metastasis to other sections of the body. Benign tumors are more likely to be cured and are relatively easier to be extracted from the body. A benign tumor is commonly surrounded by a sac and is clearly separated from normal tissues. Although benign tumors rarely develop into malignant tumors, one report indicated that around 8.6% of 186 patients who received surgical treatment for benign tumors developed breast cancer subsequently [6]. Therefore, close monitoring of benign tumors is also imperative. In contrast, malignant tumors referred to as cancers can invade surrounding normal tissues and metastasis to other body parts. Primary cancers can continue to grow and form new metastatic tumors. In comparison to benign tumors, cancers tend to be stiffer and more tightly bonded to their surroundings [7]. The way cancers evolve can make their detection and treatment difficult. A significant issue in preventing and treating breast cancers is the early detection and classification of breast tumors [1]. Tumor markers may serve a crucial function in the screening process of patients suspected of having cancer. Developing key biomarkers in strain elastography could be helpful to gain more diagnostic and prognostic information about tumors.

Current strain elastography methods have shown some promises in terms of classification [8–

10]. According to these previous studies, the classification of benign and malignant tumors is mostly governed by the tumor size and strain ratio regarding the tumor and the surrounding soft tissue. Malignant tumors appear to be larger than B-mode images. The strain ratio takes advantage of the fact that malignant tumors are more rigid than benign tumors, but some overlap exists in the criteria used for classification. Additional strain information would be beneficial to establish a greater degree of accuracy. In this context, poroelastography could be helpful by providing additional candidate parameters.

1.1.4 Poroelastography

Ultrasound elastography (EUS), initially introduced by Ophir et al. in 1991, is a widely used imaging technique to access tissue mechanical properties, including cancers noninvasively. Ultrasound elastography can be classified further as shear wave and strain elastography based on how the excitation is applied to the inspected tissue [11]. Ultrasound elastography methods examine the tissue's response using either an internal or external dynamic (shear wave based) or quasi-static (strain based) excitation. In strain elastography (SE), external compression is exerted by applying a small pressure on the tissue using the ultrasonic imaging probe. The inspected tissue will then exhibit a response to this excitation, which depends on the underlying mechanical and transport properties. For example, given applied stress, areas of hard tissue will experience less deformation than areas of soft tissue. The response of tissue to the excitation is indicated by transmission and reflection of the ultrasound waves. The ultrasonic imaging probe will collect signals according to the ultrasound waves and convert the signals to a voltage. Imaging processes are then employed to estimate the tissue displacements, strains, and related parameters with high spatial resolution. The static elastography idea proposed by Dr. Ophir's group [12] has been adopted by many medical ultrasound companies. For instance, a Hitachi EUB-8500 model uses the "Real-time Tissue Elastography" imaging technology to apply stress by hand. Likewise, Philips iU22 employs the strain based elastography by manual palpation.

Poroelastography has received increased attention in recent years as a novel subfield of ultrasound elastography [13–16]. Poroelastography quantifies the poroelastic response of a compressed tissue by utilizing temporal and spatial ultrasound strain measurements. A poroelastogram is a time series of strain images obtained while the poroelastic material is compressed [13, 17, 18]. Unlike in standard elastography methods, in poroelastography, tissue is no longer assumed to be purely elastic solid but rather a fluid-saturated material capable of translocating within a deforming solid matrix at a rate depending on permeability. Permeability is a property of the solid matrix that measures the ease of fluid flow through a porous medium [19]. Interstitial and vascular permeabilities in human tissues have been identified as contributing factors to the cancer study [20–22]. Because biological soft tissues are saturated with various fluids, it may be suitable to model tissues as poroelastic materials. When a poroelastic material is subjected to sustained uni-axial compression, the associated fluid pressure increases immediately after loading but decreases due to solid matrix deformation and fluid exudation caused by the applied stress. At a steady state, the poroelastic material performs like a linear elastic solid without fluid [23, 24]. As of today, the potentiality of poroelastography as a new tool to probe tissues' fluid mechanisms is still largely unexplored.

1.1.5 Role of Mechanical Microenvironment in Cancers

The tumor microenvironment contributes to breast tumor transformation, invasion, and metastasis. Some of the parameters that impact the tumor microenvironment are stiffness, SS, and fluid pressure [7, 23]. Of interest to this work is the investigation of interstitial fluid pressure (IFP) and solid stress (SS) that are parameters of great clinical significance for the characterization of tumors. Pathology in the body, like abnormal vasculature, lymphatic channels, and cancer growth, can lead to the presence of elevated IFP and SS [25]. IFP and SS are two distinct mechanical parameters that originate from different mechanisms and have different effects on cancer development and treatment [26].

Interstitial fluid, the body fluid surrounded by blood vessels and body cells, acts as a transport medium that carries nutrients and other vital substances produced during blood circulation [27]. Excess tissue fluid in healthy organs is typically expelled via lymphatic vessels during blood circulation as blood enters via arteries and departs via veins. In normal tissues, IFP is close to zero in most cases. The presence of a tumor disrupts the equilibrium, resulting in elevated IFP levels inside cancers. Elevated IFP is also associated with an increase in vascular permeability and damaged lymphatic system [28]. The presence of elevated IFP in cancers was first discovered in 1950 [29], and it has since then been extensively investigated theoretically, experimentally, and via simulations [30]. IFP usually drops at the cancer-tissue boundary, causing fluid flow toward lymphatic capillaries into the healthy tissue. However, clinical studies indicate that IFP can distribute heterogeneously inside the cancer [31].

Solid stress (SS), which is applied to non-fluid or elastic components of cancer, is generated by the mechanical compression or stretching of the surrounding tissue due to the proliferating and migrating cells. SS is non-uniformly distributed within the cancer [23]. SS in the primary cancers and SS in the corresponding metastasis can be dissimilar even with comparable stiffness [32]. SS might cause permanent damage even after cancer removal. Elevated SS and IFP associated with tumors can reduce vascular patency, cause poor blood supply, and significantly limit the drug delivery effectiveness [33, 34]. Non-invasive techniques to assess or quantify IFP and SS in cancers in vivo have not been established yet. In the field of elasticity imaging, SS and IFP are typically not incorporated in elastography models.

1.2 Clinical Motivation

Identification of Cancers' markers

In recent work, we explored the effect of IFP and SS on separate elastographic parameters, including axial and radial strains, volumetric strains, and fluid pressure using FEM and ultrasound simulations [35, 36]. The research in this project extends these earlier studies by investigating additional elastographic parameters as potential candidates to recognize the presence of SS in tumors.

Monitoring Tumor Progression and Treatments

Poroelastograms are composed of time-sequenced strain elastograms acquired from the poroelastic material at sampled time intervals. They provide information about the load-induced changes in the effective compressibility and fluid migration within the imaged material in a local time-dependent manner [14, 17, 18, 37]. These strain elastograms have the potential to be a useful diagnostic tool for monitoring changes in fluid patterns caused by cancer progression and treatments. Understanding fluid transport mechanisms may be crucial information for the choice of cancer treatment.

Differentiation between Malignant and Benign Tumor

Poroelastographhpy may provide additional information on the mechanical characteristics of tumors, which may aid in distinguishing between cancers and benign lesions. One part of this research investigates a novel model-based poroelastography method to distinguish benign from malignant tumors.

1.3 Objective

The objectives of this study are to:

- Construct a finite element model that accurately simulates tumor mechanical parameters and allows generation of different strain poroelastograms.
- Test Axisymmetric, 2D, and 3D tumor models.
- Generate ultrasound simulations to evaluate the performance of the computer-aided diagnosis based on the color distribution in strain elastography images.
- Investigate and analyze the impact of IFP and SS on various strains in different simulated phantoms of benign and malignant tumors.
- Identify poroelastography markers that can indicate the presence of elevated IFP and SS in a cancer.
- Utilized previously collected animal cancer data to prove the feasibility of the methods in vivo.

1.4 Structure of thesis

Chapter II examines and highlights the key concepts on poroelasticity that are pertinent to this study and provide an overview of the previously published works. Chapter III describes the design and implementation of the finite element model of benign and malignant tumors. This chapter also includes the method to generate poroelastograms of different strain components. Chapter IV reports the research outcomes and discusses critical findings on the results obtained using the FE simulation models, ultrasound simulations, in-vivo mice data, unbounded tumor, and statistical analysis. Chapter V summarizes the overall study, identifies limitations, and addresses possible future research based on the conclusions reported in this thesis.

2. LITERATURE REVIEW

2.1 Tumor Models

The mechanical behavior of tumors can be studied using analytical and numerical models. Analytical models have advantages over numerical models because analytical models allow the quantification of individual material properties. However, analytical models are not always available due to the geometry, complexity of testing conditions, and problem mechanics. In such situations, numerical simulations can be used. On the other hand, FEM, a common numerical model, sometimes fails to estimate the individual material properties because it involves minimizing several equations besides successfully meeting boundary and initial conditions. The numerical model might also suffer from algorithm non-convergence and inaccurate local minimal estimation [38].

In 1962, Biot derived the fundamental formulas for wave propagation in fluid-saturated porous media, which became known as Biot's theory of poroelasticity [39]. This theory is a foundational metric in many poroelasticity works. Eshelby (1961) provided the pioneering work on the elastic response of an inclusion embedded in an elastic material. The scholar originated the solution for the internal strains of the elastic inclusion based on the geometric shape of cancer and the background Poisson's ratio [40]. Rice et al. (1978) contributed to the field by measuring displacements, strains, and fluid pressure within a spherical porous elastic inclusion contained inside an elastic porous solid [41]. Based on these findings, our lab developed multiple analytical models for tumors with stress-relaxation or creep compression experiments [42–44].

Previous research has also provided the foundation for the numerical models of tumors in soft tissues. Baxter et al. (1989) built a 1D poroelastic model to analyze the effect of IFP on drug delivery in cancers [45]. Leiderman et al. (2006) proposed a poroelastic model that integrated interstitial and vascular permeability [46]. This research illustrated the capability of utilizing spatial-temporal strain patterns to study fluid flow. However, none of this previous work included SS and IFP in the models. Islam and Righetti (2019) adopted a novel FEM to investigate the response of normal strains, EPR, and fluid pressure of a simulated phantom to compression with the presence of IFP and SS [36]. This research aims to enhance the work of Islam and Righetti (2019) to include parameters that may affect future applications of elastography technique to cancers, particularly for cancers with known elevated IFP and SS.

2.2 Algorithms for Strain Estimation

As discussed in the previous chapter, strain elastography requires visualization of strain distribution to characterize biological tissues. Strains are derived from tissue displacement, which is estimated from radio-frequency (RF) data [47]. Multiple methods for estimating tissue strains under compression have been proposed and the fundamental idea is to minimize a cost function, which involves the displacement and radio-frequency data [48]. Richard et al. (2009) used a re-correlation method to compute strain using RF data from a phased array transducer [49]. Mohammad et.al (2012) utilized novel direct strain estimation and gradient-based strain estimation of a phantom under axial compression [50]. Omidyeganeh (2017) obtained information from RF data to generate strain elastography by using the normalized cross-correlation method [51].

Dynamic Programming is an algorithmic approach for solving issues by recursively decomposing a complex problem into simpler subproblems, and the optimum solution to the larger problem relies on each of the subproblems [52]. Horn-Schunck (HS) method is a classical algorithm to compute the displacement field by estimating the optical flow, which is a term in imaging processing to track the apparent movement of an object by observing the brightness patterns in an image [53].

Our lab recently proposed a novel two-step strain estimation technique (DPHS), which combines dynamic programming elastography (DPE) and Horn-Schunck (HS) method [17]. The proposed method employs DPE to estimate axial and lateral displacements and HS to determine the displacement field in subproblems according to RF data before and after compression. The HS method reduces the optical flow and the magnitude of flow field variations. After that, Kalman filter-based least squares estimation is performed to determine axial and lateral strains. The proposed method retains the benefits of DPE and HS while being highly efficient in terms of computation. It is expected to yield significantly higher-quality strain estimates than previous poroelastography methods [17]. This technique is utilized extensively in this project. As a result, we can visualize how local strains behave over time by poroelastograms.

2.3 Strain Imaging of Tumor

Strain imaging based on ultrasound has been investigated since the 1990s [12, 54–56]. Strain is a commonly used factor to describe the relative deformation in size and shape of materials under the application of a force. The strain tensor components comprise normal strains and shear strains. Strains that are neither normal nor shear strain are referred to as derived strains. Different from the fundamental strain components, derived strains usually include other information, such as incorporating information of tissue stiffness and tumor-tissue boundary condition [57]. In elastography imaging, the normal axial strain is frequently used because it provides information about tissue stiffness. In ultrasound elasticity imaging, the tissue is compressed utilizing the imaging transducer vertically. Axial strains are primarily used because the axial resolution of the ultrasound system is usually much higher than the resolution in the lateral and elevational direction. Thus, lateral and elevational strains estimations using ultrasound are typically much noisier than axial strains. Similarly, axial shear strain often provides superior image quality than the lateral shear strains [58].

In addition to normal strains, shear stains help to detail the near boundary bonding between stiff and soft tissues [59]. There are many factors that impact the shear strains, such as elastic modulus contrast of the material, lesion tissue boundary conditions, the amount of compression, etc. [60]. Clinically, large shear strain values can be associated with the danger of inflammation and hemorrhage [61]. Several theories have been established to estimate the normal and shear strain components [62–64]. Konofagou et al. (2000) reported on a simulation study in which elastographic images were generated from simulated data and stated that shear strain images contain clinically useful information that can be used for differentiation of breast tumor types [65]. ThitaiKumar et al. (2007) built elastic models based on axial shear strain elastography that visualized bonding conditions of a tumor to the surrounding tissue. Models were clinically matching the malignant and benign tumors of loosely and closely bound heterogeneous elements, respectively [59]. Xu et al. (2010) classified in-vivo tumors by identifying normalized axial shear strain area and suggested that axial shear strain elastography should be utilized together with axial strain elastography and B-mode imaging for breast tumor classification [66]. Thittai et al. (2011) examined the ability of normalized axial shear strain area to make tumor classification based on a broad in vivo database and recommenced including NASSA to the current standard clinical procedures [67]. A limitation of these studies is that they used only the axial component of the shear strains. To extend the previous study, Viola et al. (2002) and Rao et al. (2007) discussed the plausibility of using lateral shear strains for tissue under a uniaxial compression by signal decorrelation technique, which remarkably improved the signal-to-noise ratio of the shear strain elastography [68, 69]. Their work manifested that shear strain elastography might be used to recognize regions of increased tumor-tissue bounding.

In this study, we introduce the Von Mises strain as a potential new biomarker of tumor strain elastography. We considered the Von Mises strain as one possible candidate because it incorporates normal and shear strains in both the axial and lateral directions. As a result, a scalar representation of the tumor strain development will be generated, allowing for more precise separation of the tumor with and without SS from the surrounding tissue. Additionally, Von Mises strain is anticipated to be capable of preventing hardening and softening artifacts caused by tissue radial movement and ultrasonic beam axial prorogation [70]. Von Mises strain (Von Mises 1913) originated from the Von Mises yielding criteria and is a measure of the strain state in solids. Multiple strain components are combined in the formulation of Von Mises strain to indicate the strain-based composite failure risk [71]. There is a dearth of literature on the application of the Von Mises strain in elastography. According to Maurice et al. (2004), the Von Mises strain plays an important role as a new indicator of carotid plaque [70]. The study indicates that the Von Mises strain produces superior results compared to conventional strains (fundamental strains). Zhang et al. (2018) conducted additional clinical studies on the Von Mises strain of carotid plaque and used it to identify the risk of plaque vulnerability [72]. Ahmed A. Hameed Sayed (2013) investigated the use of Von

Mises strain for breast tumor imaging and classification using a novel 3D viscoelastic model [57]. However, this study modified the Von Mises strain equation and completely ignored the strains in the lateral direction. That is the only literature available at the moment on the Von Mises strain of tumors. In addition, this study hasn't investigated the IFP and SS. Poroelastography has not been used to study Von Mises strain results for tumors yet. We adopted the complete Von Mises strain calculation equation using a poroelastographic model to investigate the possibility of using Von Mises strain as an indicator of the presence of IFP and SS.

Principal strains must be computed in order to calculate the Von Mises strain. Principal strains are a combination of normal and shear strains that result in a maximum and minimum strain acting in principal directions on principal planes with no shear stresses [58]. This ensures all strains are normal strains. In the field of vascular elastography, principal strain imaging has been used to detect cardiac abnormalities [73–75]. Zervantonakis et al. (2007) adopted principal strain to reduce the influence of strain elastography by transducer angle and centroid ventricular [73]. Jia et al. (2009) utilized principal strain to recognize the ischemia area [74]. Nayak et al. (2017) selected principal strains to measure strain in the middle of the lumen [75]. The principal strain and the Von Mises strain are referred to as derived strains because they are determined from normal and shear strains. In general, we can see that poroelastography can be used with a wide variety of strain types. We're examining which one alters the most drastically when IFP and SS are present.

2.4 Imaging Artifacts of Strain Elastography

In strain elastography, strain patterns in the imaging are identified to obtain diagnostic information. However, the strain patterns might be corrupted by a number of imaging artifacts, especially with inappropriate elastographic procedures. Different imaging artifacts have been identified in the literature. These artifacts may impact the interpretation of the strain elastography. Hongliang et al. (2018) performed vascular ultrasound elastography to identify out-of-plane motion artifacts caused by the tissue mobility, particularly tumors with sliding boundary [76]. Barr et al. (2011) observed "bull's eye " artifacts in cystic lesions, which are induced by the fluid movement inside the cyst [77]. Dietrich et al. (2017) addressed artifacts at the border of a stiff mass contained inside the soft tissue [78].

2.5 Mechanical Parameters of Tumor

To build the FEM, previously published data on mechanical parameters for tumors are investigated to discover values of the model's input parameters. The material properties of cancers and healthy tissues have a wide range of reported values in the literature. The value of Young's modulus of cancers has been reported to be between 1.1 and 20 times that of healthy tissues [79, 80], while the value of Poisson's ratio has been reported to fall within a range of 0.2 to 0.49 for both cancers and healthy tissues [46, 81–83]. IFP levels in cancers have been reported to be between 4 and 48 mmHg [84, 85], while SS levels in cancers have been reported to be between 1.56 and 52.5 mmHg [86].

There is a limited amount of literature studying the behavior of benign tumors. The degree to which tumors bond to the adjacent tissue has been adopted as an indicator to distinguish benign tumors from malignant tumors. Hence, it is necessary to check how the unbonded case and bonded case are modeled in terms of friction. Thitaikumar and Ophir (2007) treated the tumor and tissue boundary as a contact problem with a distinct coefficient of friction μ: the loosely bounded condition assumed to have a low value ($\mu = 0.01$) while firmly bonded case assumed to have a value equal to 1 ($\mu = 1$) was considered for the firmly bonded case [54]. Xu et al. (2010) expanded the range of friction coefficient from 0.01 to 100 to represent slipping boundary and tightly connected boundary accordingly [66]. Celi et al. (2011) selected friction coefficients valued between 0 and 10 and modulus contrast between 0.5 and 7 to make the differentiation [87]. Narang (2012) pointed out that when cell to extracellular matrix adhesion or friction increased from 0.1 (weak adhesion) to 0.8 (strong adhesion), the tumor morphology was observed to change from a diffuse cluster to multiple nodules [88]. Coughlin et al (2013) used 0.1 $\sim$ 10 Pa/nm for friction with different frequencies [89]. Jiang et al. (2018) assumed a friction coefficient of 0.1 as an unbounded tumor and a coefficient of 1000 as a bounded tumor [90].

3. METHODOLOGY

This chapter will present the detailed workflow to build the finite element model, ultrasound simulations, and in-vivo experiments to study the behavior of cancer treated as a poroelastic material. This chapter also discusses a novel finite element model with friction to check the influence of tumor mobility on strain elastography.

3.1 Finite Element Simulation

Phantom Geometry

The finite element method (FEM) is recognized as a powerful technique for assessing the strain behavior of various lesions using poroelastography. The fundamental steps of FEM usually involve constructing the model's geometry, specifying material characteristics, defining physics, meshing the geometry, numerically solving the system of equations, and post-processing results. This research uses a leading commercial FEM software named ABAQUS. This software enables the simulation of complex problems, such as the strain states induced in mechanical loading situations. A proper workflow has been established using ABAQUS.

A geometric description of a tumor is necessary to build a FEM model. A schematic illustration of the sample configuration utilized in this research is shown in Fig. 3.1. The dimensions of the sample were set as a cylinder with a 2 cm radius and a 4 cm height [35, 36]. As for tumors, they can be of many shapes because each tumor is uniquely grown, which means that the shape of a tumor varies and is unpredictable. For simplicity, poroelastic samples with spherical and elliptical inclusions are assumed in this study as these two shapes cover most of the clinical cases. The elliptical inclusion is assumed to have zero rotation, which guarantees the symmetric nature of the model and allows axisymmetric assumption. The spherical tumor is assumed to have a radius of 0.75 cm. For the elliptical tumor, the half of the minor axis of the tumor is specified to be 0.375 cm with an aspect ratio of 1.429. The model is under constant uniaxial compression on the top and has a fixed axial displacement at the bottom. The compressor plate used to support and compress the sample is assumed to be frictionless.

This study primarily considers the axisymmetric model because it has acceptable computational speed and contains sufficient information. Two-dimensional and three-dimensional models are also created to increase the adaptability of the current design and may be used in the future. The results are anticipated to be the same. The two-dimensional model further reduces the computational cost and allows retrieving strain poroelastography images more efficiently. The three-dimensional model can help make a more comprehensive overview by collecting all needed information while not having the axisymmetric model's limitation. In this study, a three-dimensional model is used to confirm the signs of asymmetric shear strains.

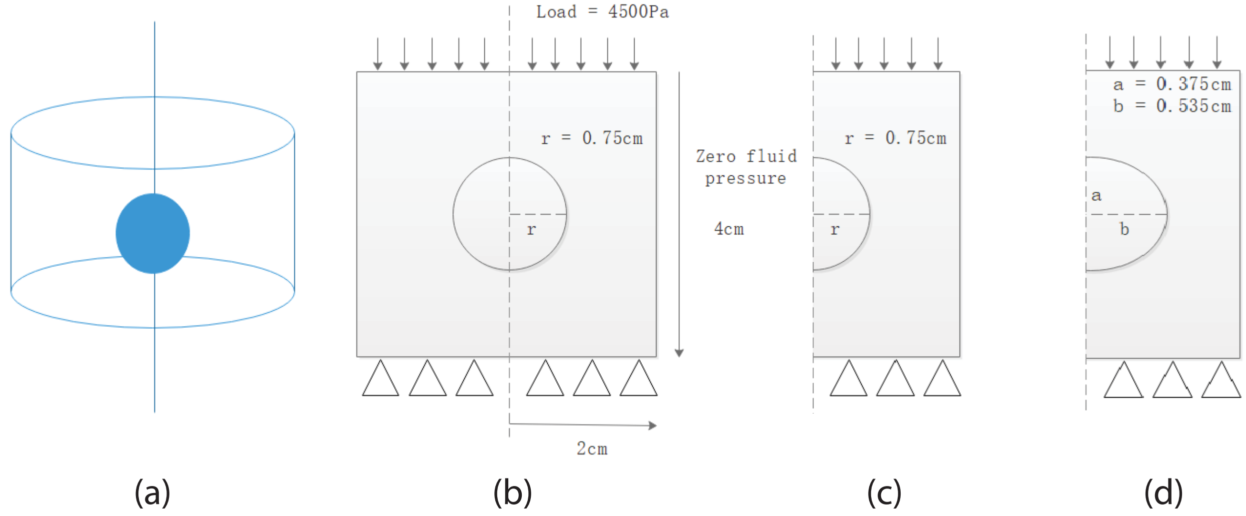

Figure 3.1: A schematic illustration of the (a) 3D model, (b) 2D cross section, and (c)asymmetric of a cylindrical sample with spherical inclusion. (d) axisymmetric solution plane of a cylindrical sample with elliptical inclusion.

Assumptions

With respect to the feasibility and the necessity of the finite element model, certain assumptions are needed:

1. The shape of the tumor is spherical or elliptical to enable axisymmetric modeling [35, 36].

The axisymmetric model assumes Equal lateral and elevational strains.

2. All materials are assumed to be poroelastic, which allows the application of biphasic theory. The solid phase is assumed to have linear stress-strain behavior and to be fully saturated with a single darcy fluid flowing through the medium following Darcy's law [35, 36].

3. The input parameters, including mechanical and transport properties, are uniformly distributed and remain constant in the tissue and background throughout the elastography experiment.

4. The IFP is assumed to be an isotropic stress with zero shear components [25] while the SS is assumed to be anisotropic with zero shear components [91, 92]. The isotropic stress vector contains equal axial, radial, and tangential components. Both IFP and SS remain constant throughout the elastography experiment.

5. Thermal effects, dynamic effects, and other effects are ignored, and the potential influences on the strains are not investigated.

6. In addition, there is an assumption of firmly bonding boundary conditions for malignant tumors and loosely bonding for benign tumors [54, 66, 87, 88, 90]. Abaqus allows users to define contact interactions and assign a friction coefficient to represent the bonding condition. The coefficient that is close to zero illustrates a loosely bonding. The larger the coefficient of friction, the more firmly the bonding is.

Governing Equations

This project utilizes the 'coupled pore fluid diffusion and stress analysis' module of ABAQUS, which integrates a system of governing equations to describe the physics of the coupling fluid and solid. More details can be found in the ABAQUS documentation. When fluid exudes the sample due to compression, the fluid saturating the pore will have decreasing pressure. The reduced fluid pressure may induce tissue compaction. The fundamental law governing this phenomenon is the effective stress principle for porous media, which specifies that the total stress acting on a point is the combination of the effective stress on the solid matrix and the average fluid pressure [93]. This equation governs the mechanical part of the porous media because the effective stress is a crucial parameter to evaluate changes in compression, deformation, and shear resistance [94]. The effective stress is given by:

$$\boldsymbol{\sigma}_e = \boldsymbol{\sigma} + p\boldsymbol{I}. \tag{3.1}$$

where $\boldsymbol{\sigma}_e$ is effective stress or elastic stress on a solid matrix, $\boldsymbol{\sigma}$ is total stress acting at a point, p is pore pressure or average wetting fluid pressure, and $\boldsymbol{I}$ is the identity matrix.

Another significant governing equation is the continuity equation, also known as material balance equation. The continuity equation is a quantitative representation of the mass conservation principle. Backward Euler method, a well-known numeric method, is used to solve the continuity equation and the combined formula can be written as:

$$\int_V \left[\delta p\big((\rho_w n_w)_{t+\Delta t} - \frac{1}{J_{t+\Delta t}}\big(J\rho_w n_w\big)_t\right] dV + \Delta t \int_V \delta p \left[\frac{d}{d\boldsymbol{x}} \cdot (\rho_w n_w \boldsymbol{v}_w)\right]_{t+\Delta t} dV = 0, \tag{3.2}$$

where ρ_w is the mass density of the liquid, n_w is the volumetric ratio of wetting liquid to the elementary volume $n_w = \frac{dV_w}{dV}$, $\boldsymbol{v}_w$ is the average velocity of the wetting fluid relative to the solid phase, t is the time domain, x is the space domain, and J is the ratio of the material's volume in the current configuration to its volume in the reference configuration $J = \frac{dV}{dV^0} \sim 1 + div(\mathbf{u})$, where $\mathbf{u}$ is the solid phase displacement vector [93].

Darcy's law describes the flow of a fluid through a porous medium and has the following equation [93]:

$$n_w \boldsymbol{v}_w = \frac{-k}{\gamma_f} \nabla p, \tag{3.3}$$

where k is the interstitial permeability of the solid phase and γ_f is the volumetric weight of pore fluid.

Loading and Boundary Condition

A constant vertical pressure of 4500 Pa is prescribed on the top of the cylindrical sample. The boundary condition at the bottom is with zero axial displacements. The fluid pressure is assumed to be zero at the sample's right boundary [95]. The boundary conditions indicate that the fluid cannot flow from the upper and lower edges but can flow radially outward from the center.

Initialization/Modeling the IFP and SS

When inputting initial stress in ABAQUS, the finite element model may fail to reach the equilibrium state. Thus, a small initial step is necessary to achieve the equilibrium [93]. An initial time step of 0.01 s is prescribed in this study, and the load is applied in 0.01 s. The experiment ends at 60.01 s, but the total poroelastic response recording period is 60 s at 10 fps (frames per second). "Soils consolidation" is a step type used to define a step in which fluid is meant to flow and settle. The steps are defined as "soils consolidation" to allow fluid to flow over time steps. The IFP and SS were modeled in ABAQUS using the pre-defined stress field that requires the input of six components. The first three components are normal axial, radial, and elevational stresses, and the last three components are shear stresses. The shear components are assumed to be zeros. Due to the anisotropic nature of SS and the isotropic nature of IFP, the normal axial, radial, and elevational stresses differ for SS but are equal with the value of -P for IFP.

Material Properties Specification

A variety of simulated phantoms with different properties of backgrounds and inclusions are simulated. Table 3.1 reports a summary of the simulation cases analyzed in this study. The cases are carefully selected to identify the difference with the presence of IFP and SS. The Property Module in the Abaqus/CAE and the input file (.inp) require modification to input material properties. In the Property Module, the material behaviors used are "elastic" and "permeability". The primary input data for the elastic section are Young's modulus and Poison's ratio, while the primary input data for the permeability section are the specific weight of the fluid, interstitial permeability, and void ratio. Previous literature indicates that the material properties of cancer and tissue are wide-ranging [46, 79–83]. Normal tissue is assumed to be nearly incompressible, with a Poisson's ratio of 0.49 and Young's modulus of 32780 Pa. The tumor is assumed to be compressible with a Poisson's ratio of 0.3 and Young's modulus of 54990 Pa. All samples have the specific weight of the wetting liquid of 1Nm-3 and a void ratio of 0.4 [42]. We note that ABAQUS uses the hydraulic conductivity (k_A), which is equal to permeability (k) multiplied by the specific weight of the wetting liquid (γ). The equation is shown below [93].

$$k_A = k\gamma_w, \tag{3.4}$$

Pore fluid flow in ABAQUS is specified as seepage flow by defining seepage coefficients in consolidation analysis for each element. In this study, the seepage coefficient is used to control vascular flow from the interior to the exterior and is inputted in analysis by using the "FLOW" keyword. User subroutine FLOW is not supported in ABAQUS/CAE, which is the visualization work platform of the software. ABAQUS/CAE generates the input file (.inp), and users need to modify the input file to use FLOW by following the format described in ABAQUS documentation. The vascular permeability is defined in FLOW.

Meshing

Meshing type and element size should be carefully determined. A sufficient number of elements or a finer mesh are crucial to image accuracy and to prevent the locking phenomenon for nearly incompressible materials. Computational time and resources will be traded off to war-

Sample	E_b (kPa)	E (kPa)	ν_b	ν	k_b (m^{4}N^{-1}s^{-1})	k (m^{4}N^{-1}s^{-1})	χ_b $(Pa*s)^{-1}$	χ $(Pa*s)^{-1}$	S_a	S_r	S_t	P
A	32.78	54.99	0.49	0.3	6.4×10^{-15}	3.1×10^{-14}	5.4×10^{-8}	2.79×10^{-6}	0	0	0	0
B	32.78	54.99	0.49	0.3	6.4×10^{-15}	3.1×10^{-14}	5.4×10^{-8}	2.79×10^{-6}	0	0	0	5
C	32.78	54.99	0.49	0.3	6.4×10^{-15}	3.1×10^{-14}	5.4×10^{-8}	2.79×10^{-6}	14.1	16.9	0.17	0
D	32.78	54.99	0.49	0.3	6.4×10^{-15}	3.1×10^{-14}	5.4×10^{-8}	2.79×10^{-6}	14.1	16.9	0.17	5

Table 3.1: The input parameters of the simulated samples A-D. E, ν and k are the Young's modulus, Poisson's ratio and interstitial permeability, respectively. The parameter $\chi = \frac{L_p S_v}{V_v}$, where L_p is the vascular permeability and $\frac{S_v}{V_v}$ is the surface area to volume ratio of the capillary walls. The subscript b refers to the parameters in the background region while the parameters without subscript correspond to the inclusion region. S and P denote the SS and IFP inside the tumors with a unit of mmHg. Subscripts a, r and t denote the axial, radial and tangential components, respectively.

rant enough elements. The axisymmetric model uses 4-node axisymmetric bilinear displacement and pore pressure with reduced integration and hourglass control, known as CAX4RP. Reduced integration is an improved approach used to minimize the amount of calculation required, thus reducing data storage. This procedure can be used for quadrilateral elements. Reduced-integration elements require fewer points of integration in each direction than fully integrated elements. The integration points, so-called Barlow points, are located at the place where the highest precision of the element is achieved [96]. The stiff matrix is often overestimated in finite element formulation, and using fewer integration points should result in a less stiff element. As a result, reduced integration is preferable to full integration in some situations, especially with creep or incompressible material problems. The reduced integration decreases the time to run and is more suitable for the second-order elements due to better accuracy [93].

A particular procedure is required for the axisymmetric model to make the mesh successfully. The model used rectangular partition inside and outside the tumor, as shown in Fig. 3.2, to ensure that square mesh elements have an aspect ratio of 1. This partition is critical because ABAQUS calculates the seepage coefficient for each mesh element, which requires equal length to achieve the same vascular permeability throughout the inclusion or background. The element shape must be set as "Quad" to avoid a triangle shape. While meshing the sample geometry, no mesh refinement is deployed in this study. As a result, 81492 elements were generated in the solution plane.

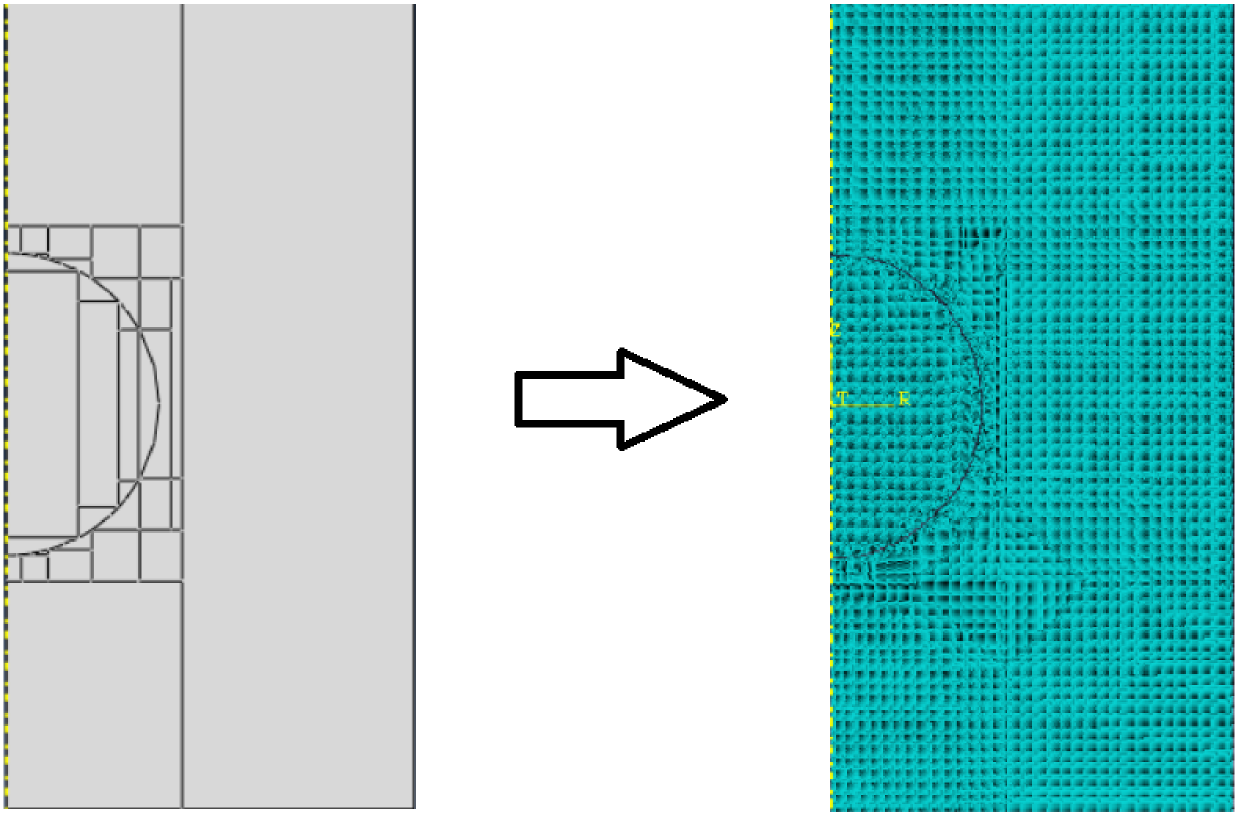

Figure 3.2: Finite element model with partition and corresponding mesh

Simulation of Benign and Malignant Tumors

For the malignant tumor modeling, the tumor and the background interface are assumed to have no friction. This model is realized from a modeling perspective by merging the inclusion and background parts in ABAQUS. In this way, fully bonded is ensured. The benign tumor modeling involves contact with friction. Surface to surface contact is used in ABAQUS. Contact calculation requires identifying a master surface and a slave surface. Nodes on the slave surface are prohibited from penetrating the master surface, but nodes on the master surface can penetrate the slave surface. In this study, the tumor surface is identified as the master surface. The part of the tissue that is in contact with the tumor is identified as the slave surface. The relative tangential displacement of the two surfaces is controlled by specifying the contact as "finite sliding" or "small sliding." Finite sliding, which this study utilizes, is commonly used with greater computational demands. Small sliding is preferred if the distance between two neighboring nodes seems to be larger than the relative tangential displacement. The contact module also requires inputs of the interaction properties. Tangential behavior, also recognized as the frictional behavior in this study, is selected to control the contact. There are various friction formulations to describe frictional behavior. Penalty friction formulation is used to model benign tumors. When using penalty friction formulation, the isotropic frictional property is used by default in ABAQUS. The friction coefficient is changed accordingly from case to case.

Simulation Output

The primary outputs are axial and radial displacements. MATLAB is used to import the displacement data from ABAQUS data file (.dat) and compute different strains elastograms, such as axial strain, lateral strain, axial shear strain, lateral shear strain, total shear strain, first principal strain, second principal strain, and Von Mises strain and corresponding poroelastograms. The overall procedure is shown in Fig. 3.3. The derived strains are calculated on a pixel-by-pixel basis.

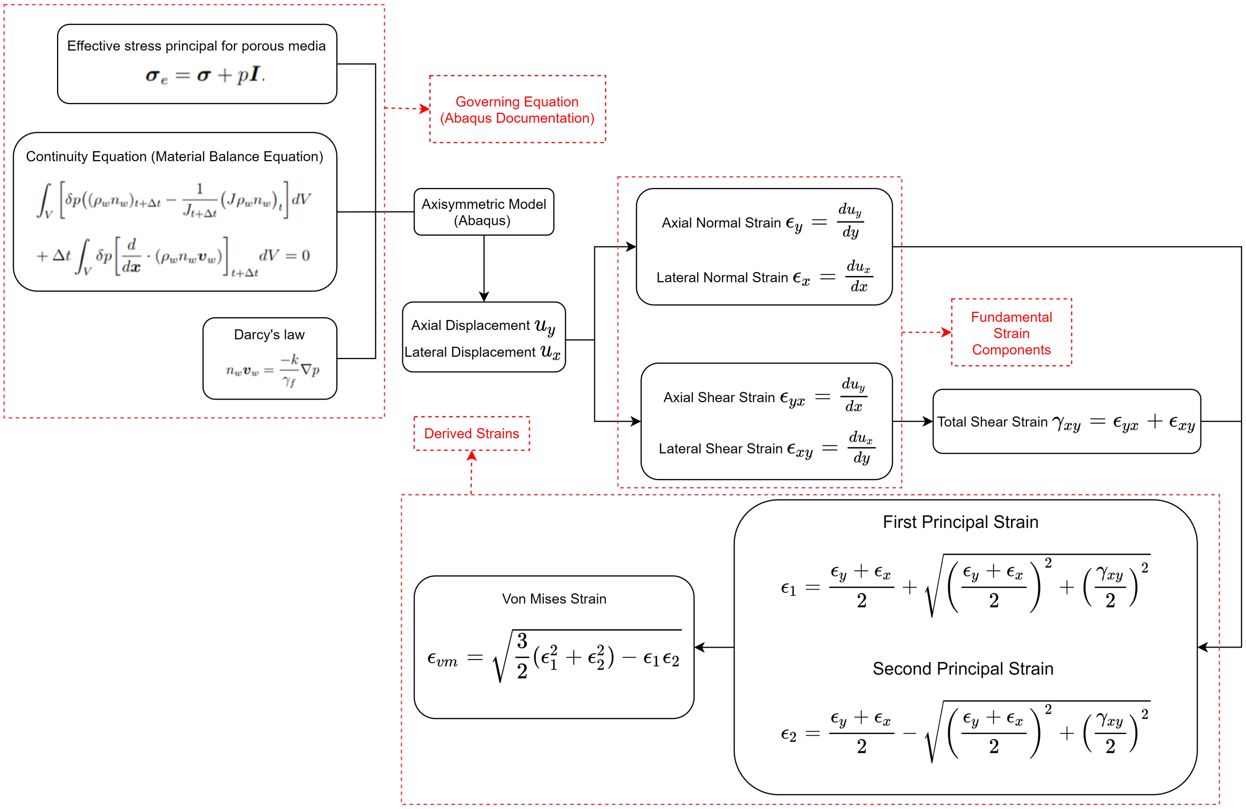

Figure 3.3: Flow Chart used for the computation of the various strains utilized in this project.

3.2 Ultrasound Simulation

The performance of the proposed technique is evaluated using ultrasound simulations data In one selected case (Sample D). Fig. 3.4 illustrates procedures of ultrasound simulation and specifications of the simulated ultrasound transducer, which resembled our experimental transducer. A convolution model, in which the object field is convolved with the transducer's point spread function (PSF), processes FEM nodal displacements to obtain the simulated ultrasound RF data before and after compression [97, 98]. The RF data integrates the Gaussian noise of a particular SNR that is subjective to the measurement and electronic noise before and after compression. The scattering distribution is supposed to be a Gaussian distribution with zero mean and unit variance [13]. From the simulated RF data before and after compression, axial and radial displacements and strains were obtained using the DPHS technique recently developed in our lab [17].

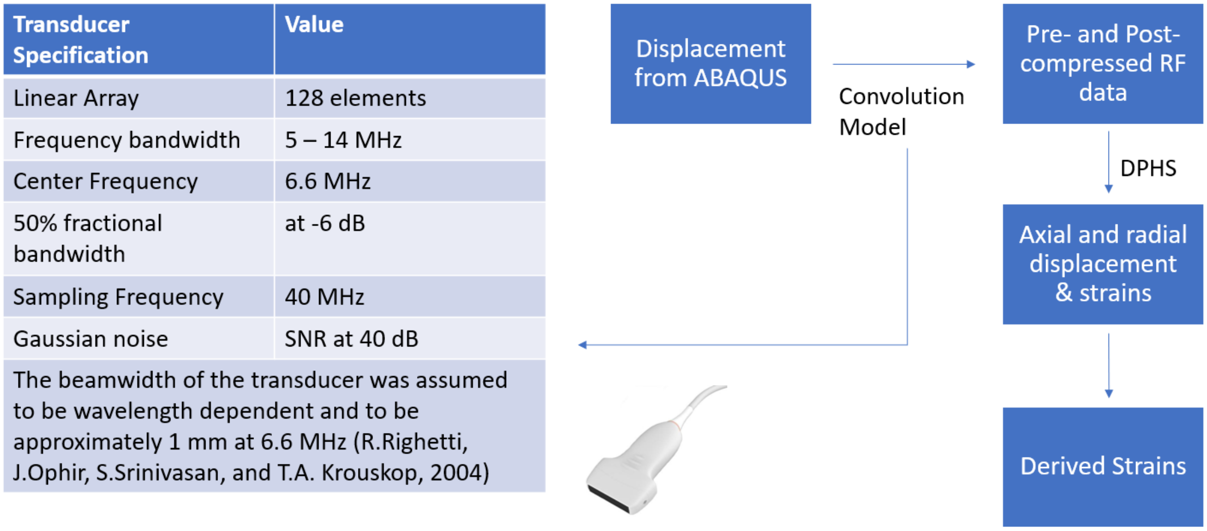

Transducer Specification	Value
Linear Array	128 elements
Frequency bandwidth	5 – 14 MHz
Center Frequency	6.6 MHz
50% fractional bandwidth	at -6 dB
Sampling Frequency	40 MHz
Gaussian noise	SNR at 40 dB
The beamwidth of the transducer was assumed to be wavelength dependent and to be approximately 1 mm at 6.6 MHz (R.Righetti, J.Ophir, S.Srinivasan, and T.A. Krouskop, 2004)	

Figure 3.4: Flow Chart used for the ultrasound simulation to generate displacements and strains and the ultrasound specification in this project [17, 99].

3.3 Animal Cancer Study

Previously acquired experimental data from animal cancers was analyzed with the intent of: (A) demonstrating the technical feasibility of creating derived strain elastograms (first principal, second principal, and Von Mises) from experimental data in vivo and (B) experimentally validating some of the strain patterns observed in the simulation results, i.e., specifically changes in the derived strain distributions with the onset of cancer and ostensibly related to an increase of IFP and SS. The cancers were created in a small animal model by injecting cancerous cells under the mice's mammary fat pad. A gel pad is applied to the mice during data collection, which has no discernible effect on the stress distribution inside the sample, and therefore does not affect the computed strains [79]. The database consisted of six untreated malignant cases, with three from 2017 with labels M324, M326, M347, and three from 2019 with labels M14, M5, M24. No data on benign cases was available. Consequently, the data were used mainly as a proof-of-principle of the proposed technology. The procedures of mice data processing are shown in Fig. 3.5.

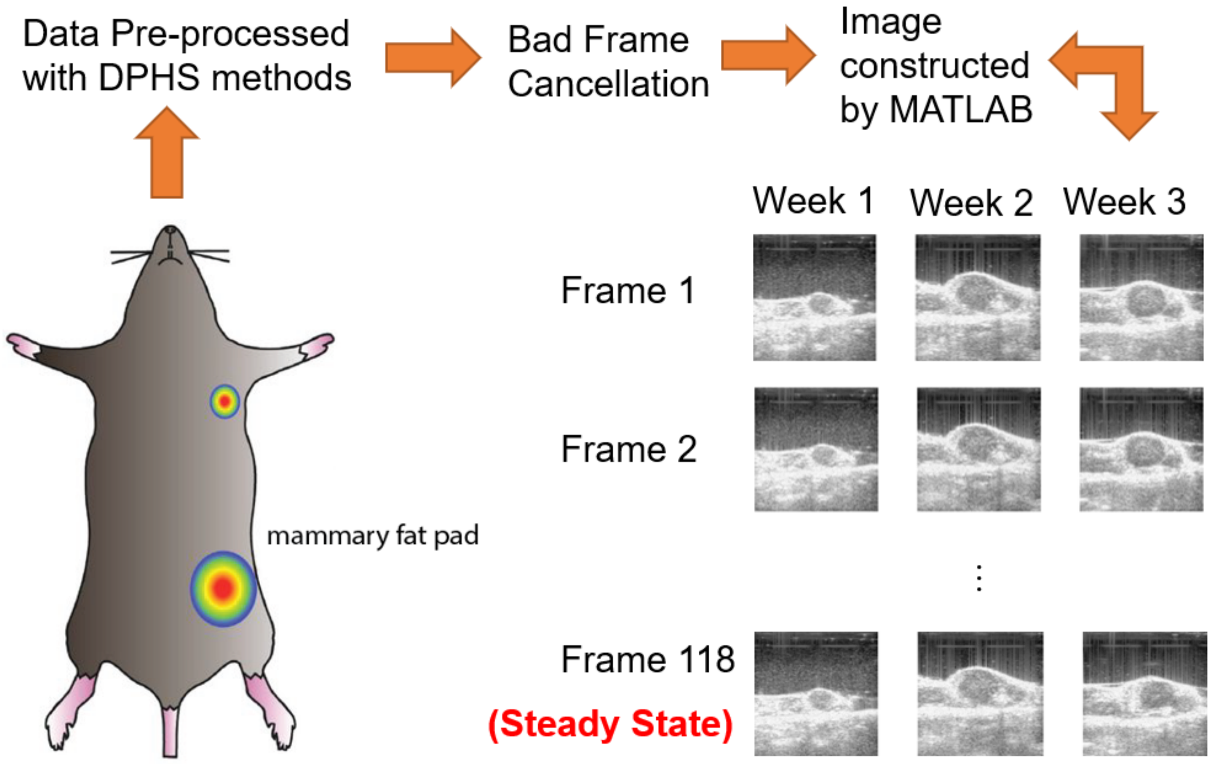

Figure 3.5: Demonstration of the Mice data process. The depiction of the mice is obtained in Chenchen Pan et al. (2019) [100].

3.4 Statistics Consideration

Statistical analysis was performed on the various simulated phantoms to detect differences in the poroelastographic parameters. The statistical analysis focuses on inclusion since it is the region of interest. The selection of statistical tests relies on the normality of the data since many models assume a normal distribution.

4. RESULTS AND DISCUSSION

In this chapter, the results from the studies will be presented.

4.1 Malignant Tumor

4.1.1 FE Simulation

The axial shear strain poroelastograms in samples A-D are shown in Fig. 4.3. As observed in the figure, the axial shear strain does not vary significantly over time with or without the presence of IFP and SS. Besides this, axial shear strains within the inclusion are zero in samples A and B, demonstrating that IFP does not produce any axial shear strain in cancer. On the contrary, in samples C and D, where SS occurs, the axial shear strain is non-zero in cancer with alternating polarity. We observe that the axial shear strain has alternating polarity at the background/inclusion interface. The pattern has the same sign diagonally; this is also true for radial shear strain. This finding is consistent with the previous study [59].

The poroelastograms of radial shear strain in samples A-D are displayed in Fig. 4.4. Like the axial shear strain, the radial shear strain does not change substantially over time in all samples and is zero within the inclusion in samples A and B. We can see higher radial shear strains in samples C and D at the background/inclusion interface, which demonstrates that SS generates radial shear strain as well as axial shear strain inside the inclusion while the IFP does not. However, the changes in shear strains occur primarily at the background/inclusion interface. Even if these strains are non-zero inside the inclusion in the presence of SS, these strains are still very small.

Turning now to the results on derived strains, Fig. 4.5 presents the first principal strain poroelastograms for samples A-D. In sample A, the first principal strain increases from 9.5% to 10.5% at the steady-state. In sample B, the first principal strain is reduced to about 9.7% at the steady-state. In samples C and D, the first principal strain decreases within the inclusion. The first principal strain is spatially uniform within the inclusions in samples A and B and spatially dependent within the inclusions in samples C and D. In general, IFP and SS seem to reduce the first principal strain in cancer.

The second principal strain poroelastograms highlight a more noticeable change in the different samples as shown in Fig. 4.6. The figure depicts approximately -4.6$\%$ initial value and -3.8$\%$ at steady-state inside the inclusion in sample A. In sample B, because of IFP, the second principal strain reaches around -4.3

The Von Mises strain poroelastograms for samples A-D at different time points are shown in Fig. 4.7. From the figure, it is hard to discern variations in the Von Mises strain over time visually. For samples C and D, the Von Mises strain has a lower value in the central part of the inclusion than in the peripheral part of the inclusion and forms a gradient inside the inclusion. Von Mises strain is space-dependent with the existence of SS, like principal strains.

The temporal profiles of the absolute axial shear strains at five different points inside the inclusions in samples A-D are shown in Fig. 4.9. These five points include the center point and four points located near the tumor-tissue boundary at different radial distances from the center. We see from Fig. 4.9 that, overall, the axial shear strain is very small inside samples A and B. Axial shear strain is more visible in samples C and D because of the presence of SS. Radial shear strain also is very small (≈ 0) in samples A and B while more changes are identified in samples C and D (shown in Fig. 4.9). For the first principal strain, We see that it both starts at a value around 9.5% and increases in samples A and B. In samples C and D, the first principal strain starts to decrease with time due to the presence of SS. For the first principal strain, both the existence of IFP and SS would appear to reduce the first principal strain. The second principal strain decreased in the presence of IFP but increased in the center with SS. Von Mises strain changed slightly with time with the presence of SS and IFP in samples A and B but changed drastically in the center. We also observe the spatial dependent pattern for the derived strains by comparing the inclusion to the background.

The elliptical tumor inclusion, as shown in Fig. 4.8, has also been modeled for our purposes. The primary observation is that the trend of strain distribution in elliptical tumors is qualitatively similar to that in spherical tumors, with slight differences due to geometry. As a result, we anticipate that these findings will hold for both spherical and elliptical tumors under realistic experimental conditions. The orientation of the elliptical tumor might influence the results, but this is left for future work.

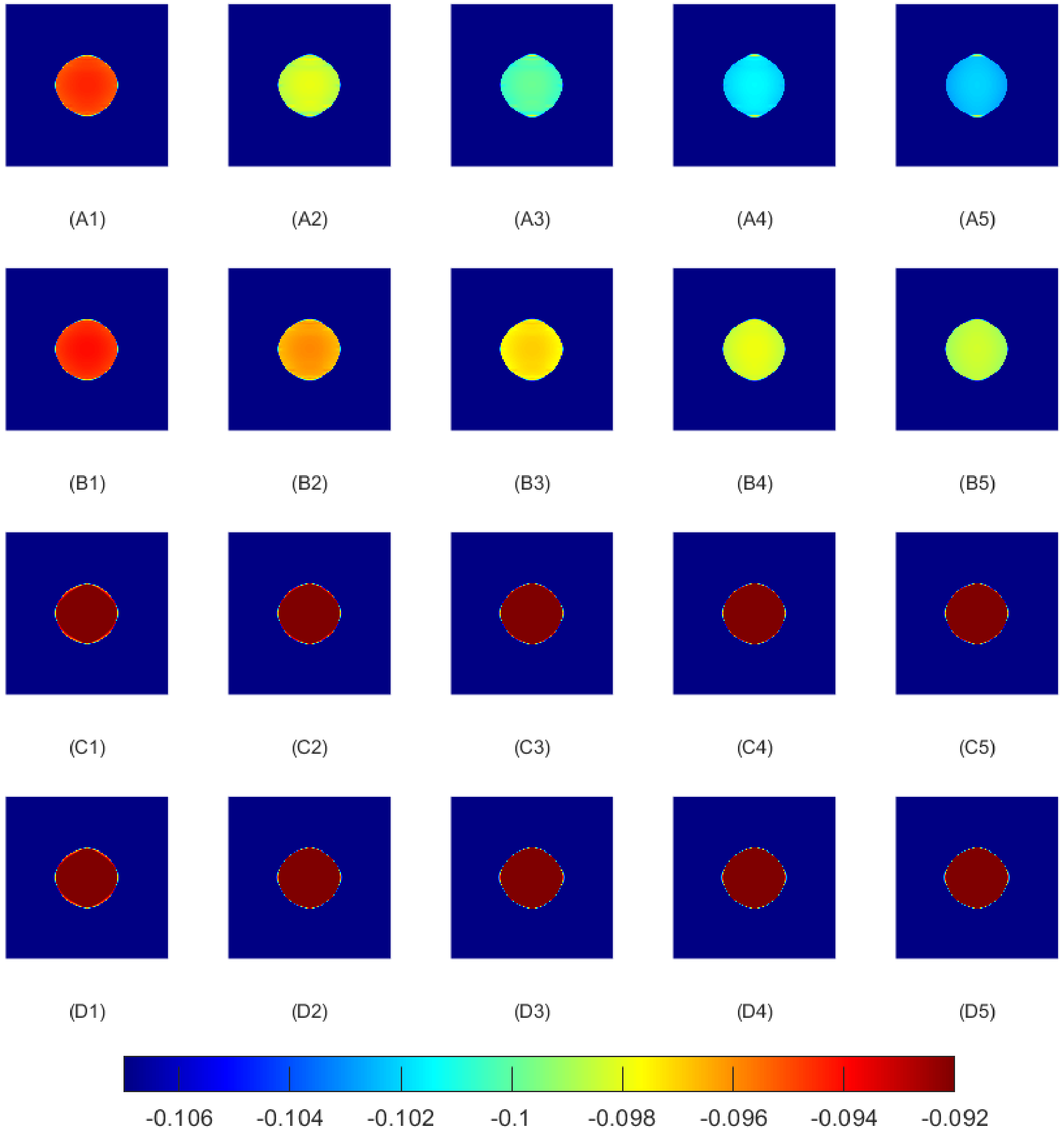

Figure 4.1: Axial strain at time points of 0.6 s (0^+ s), 4.8 s, 9 s, 18 s and 57.6 s for samples A, B, C and D are shown in (A1-A5), (B1-B5), (C1-C5) and (D1-D5), respectively.

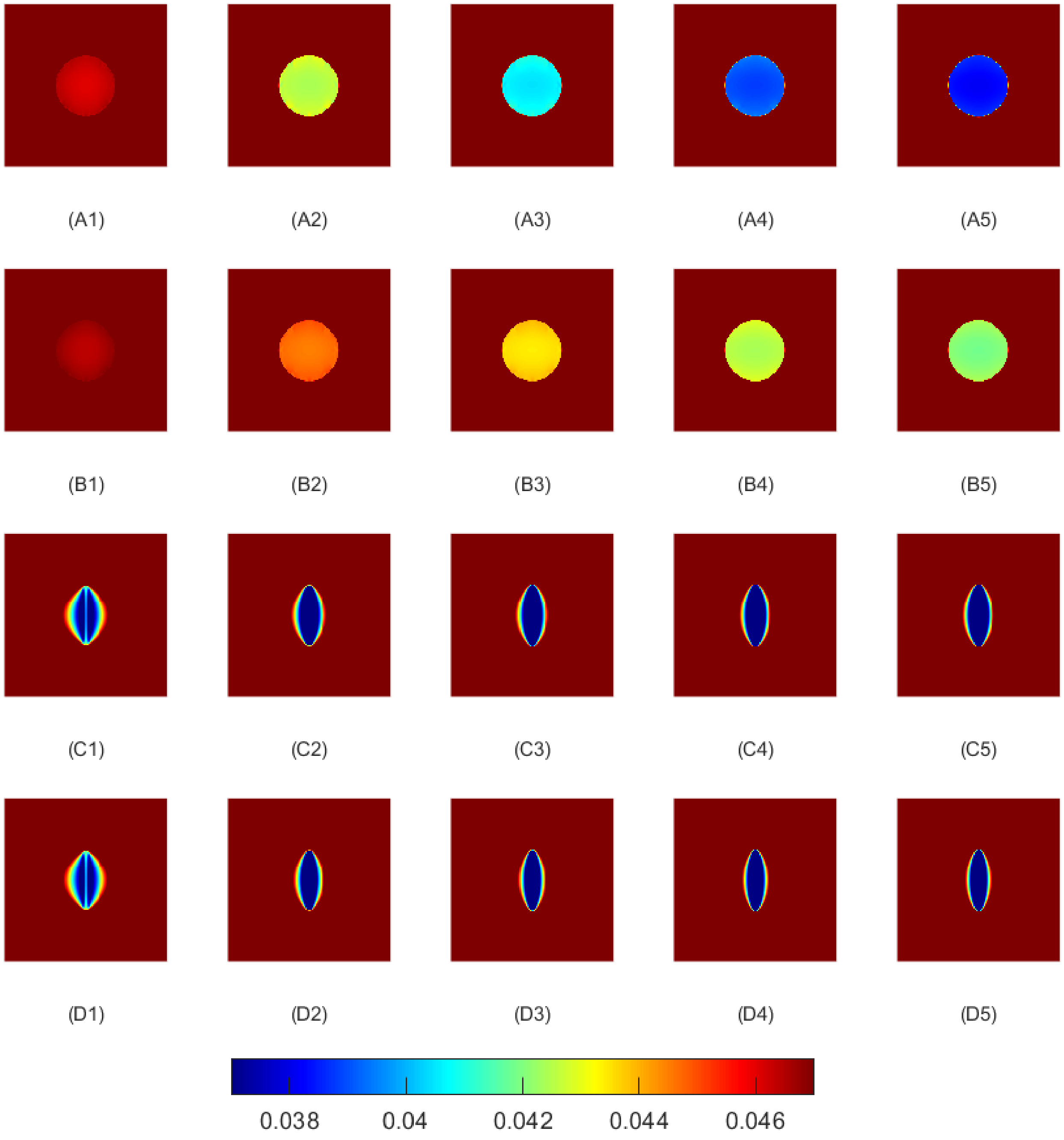

Figure 4.2: Radial strain at time points of 0.6 s (0^+ s), 4.8 s, 9 s, 18 s and 57.6 s for samples A, B, C and D are shown in (A1-A5), (B1-B5), (C1-C5) and (D1-D5), respectively.

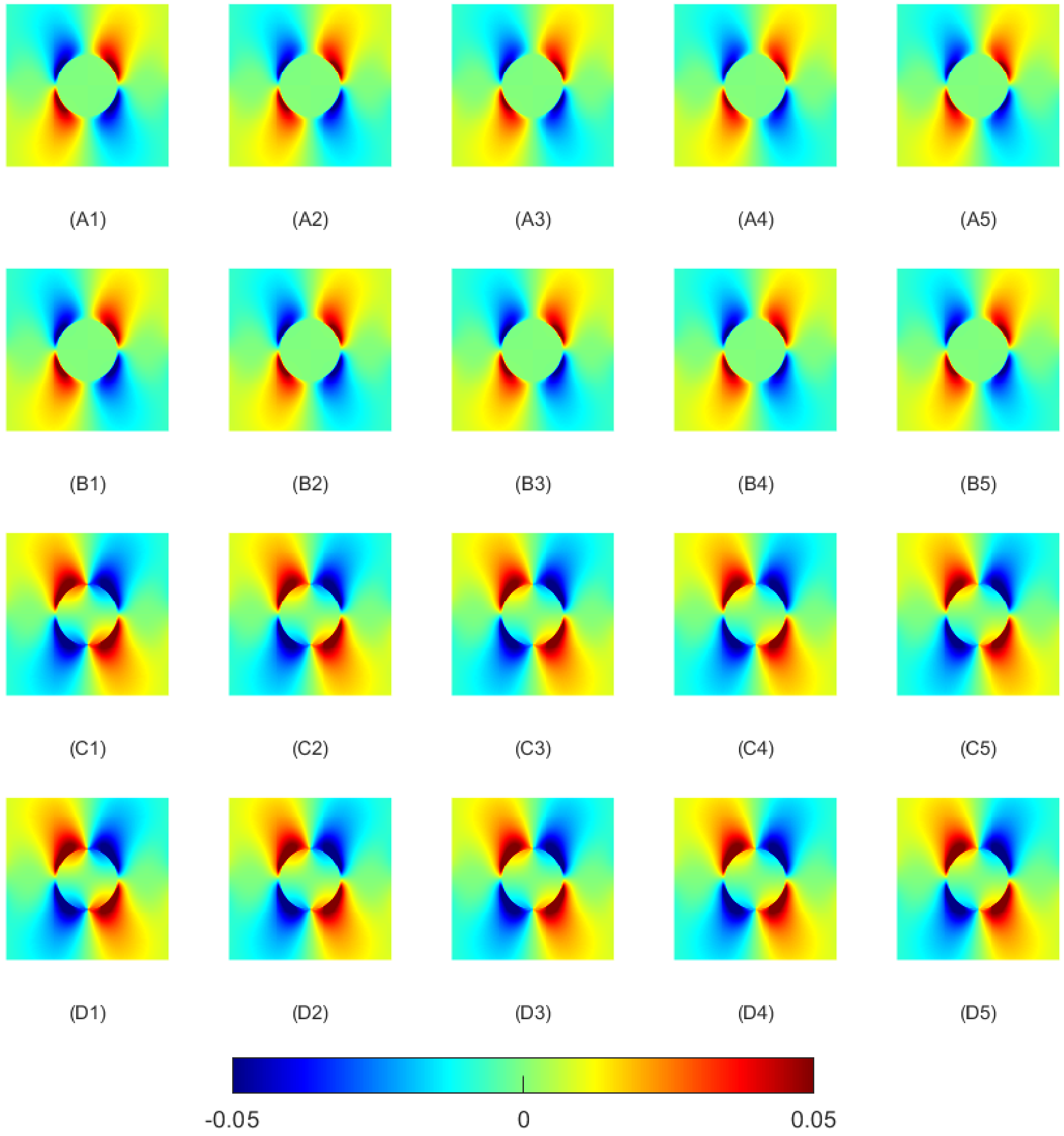

Figure 4.3: Axial shear strains at time points of 0.6 s (0^+ s), 4.8 s, 9 s, 18 s and 57.6 s for samples A, B, C and D are shown in (A1-A5), (B1-B5), (C1-C5) and (D1-D5), respectively.

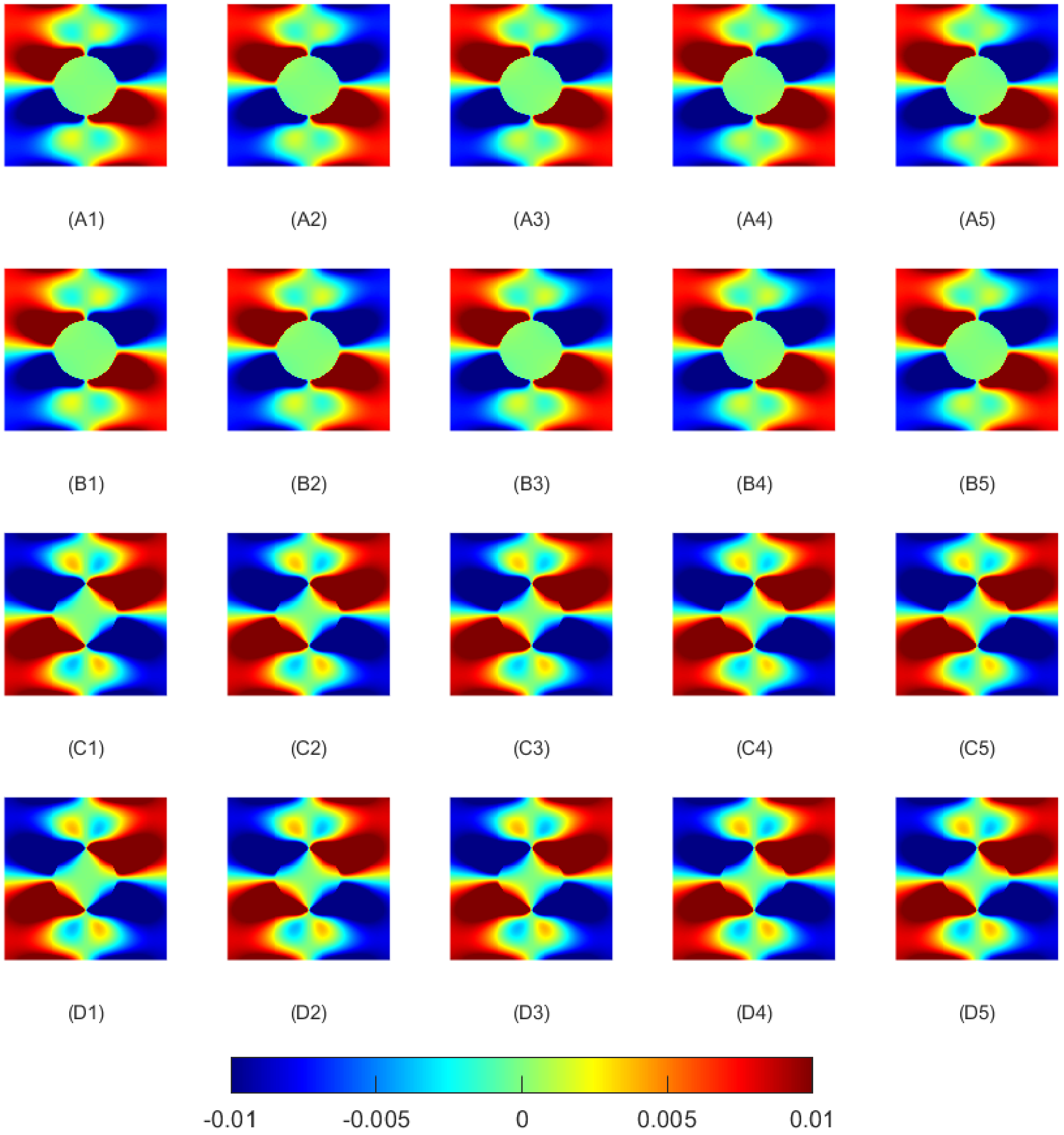
(A1) (A2) (A3) (A4) (A5)

(B1) (B2) (B3) (B4) (B5)

(C1) (C2) (C3) (C4) (C5)

(D1) (D2) (D3) (D4) (D5)

Figure 4.4: Radial shear strains at time points of 0.6 s (0^+ s), 4.8 s, 9 s, 18 s and 57.6 s for samples A, B, C and D are shown in (A1-A5), (B1-B5), (C1-C5) and (D1-D5), respectively.

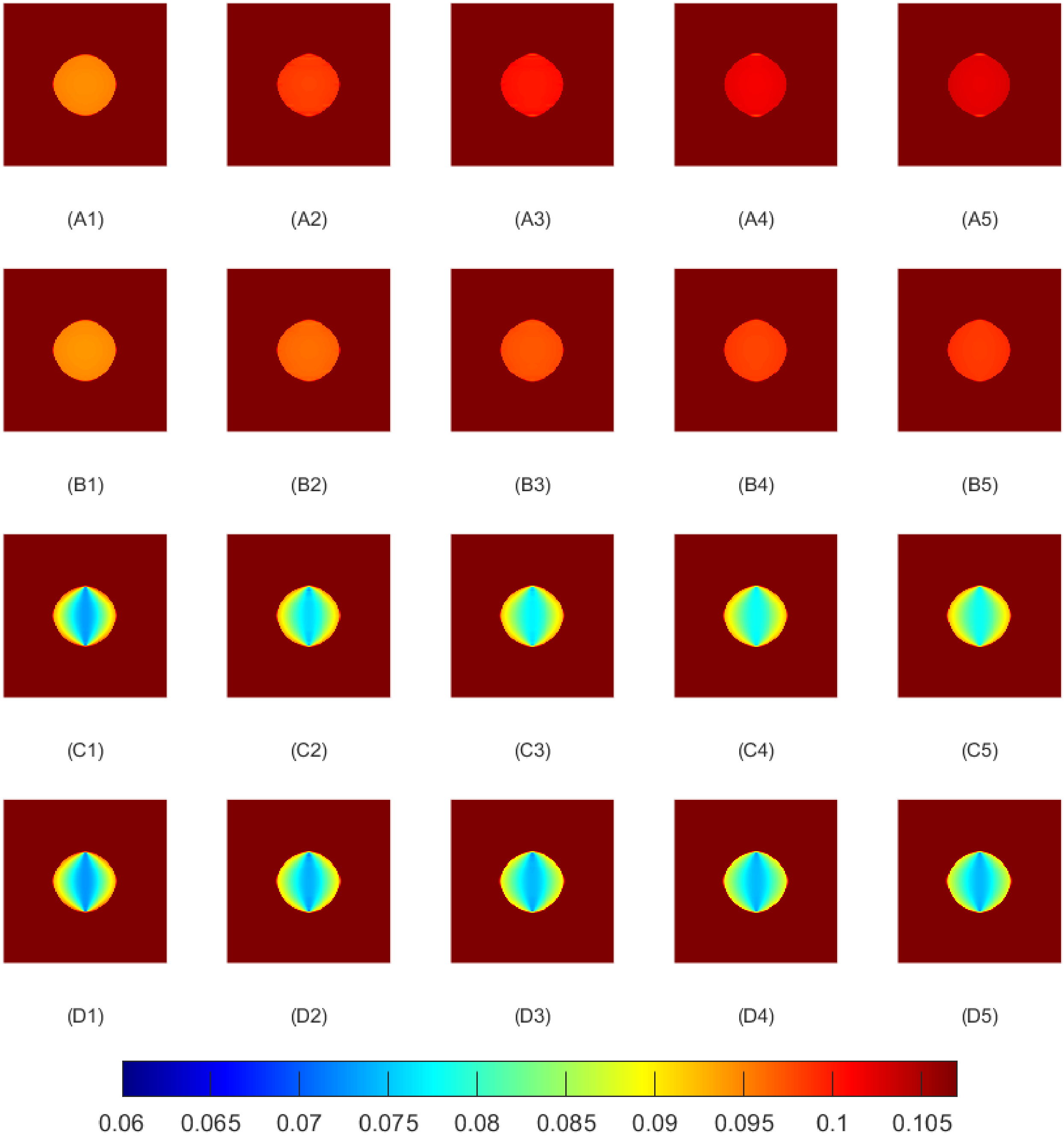
(A1) (A2) (A3) (A4) (A5)

(B1) (B2) (B3) (B4) (B5)

(C1) (C2) (C3) (C4) (C5)

(D1) (D2) (D3) (D4) (D5)

Figure 4.5: First principal strain at time points of 0.6 s (0^+ s), 4.8 s, 9 s, 18 s and 57.6 s for samples A, B, C and D are shown in (A1-A5), (B1-B5), (C1-C5) and (D1-D5), respectively.

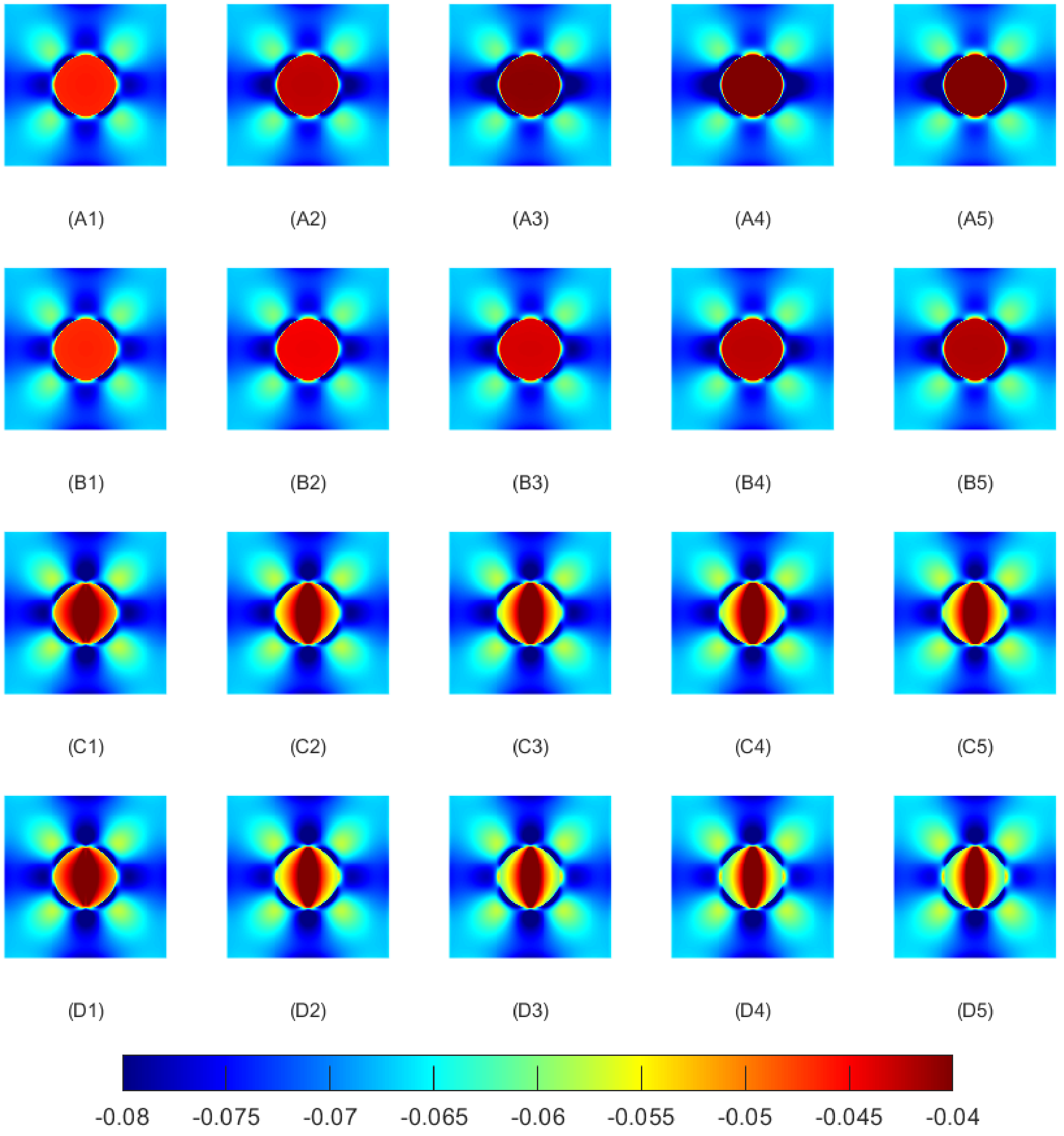

Figure 4.6: Second principal strain at time points of 0.6 s (0^+ s), 4.8 s, 9 s, 18 s and 57.6 s for samples A, B and C are shown in (A1-A5), (B1-B5) and (C1-C5), respectively.

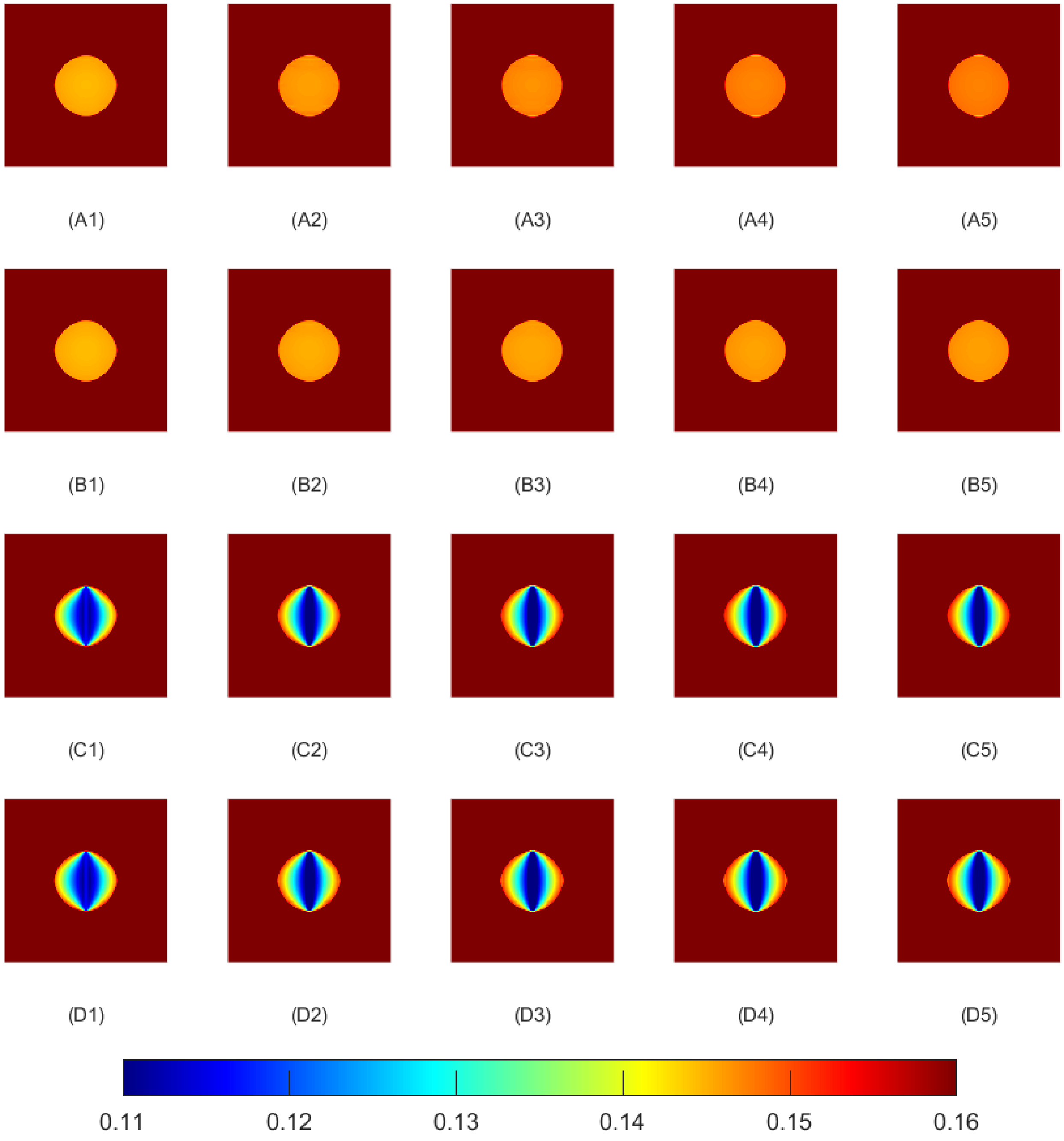

Figure 4.7: Von Mises strain at time points of 0.6 s (0^+ s), 4.8 s, 9 s, 18 s and 57.6 s for samples A, B, C and D are shown in (A1-A5), (B1-B5), (C1-C5) and (D1-D5), respectively.

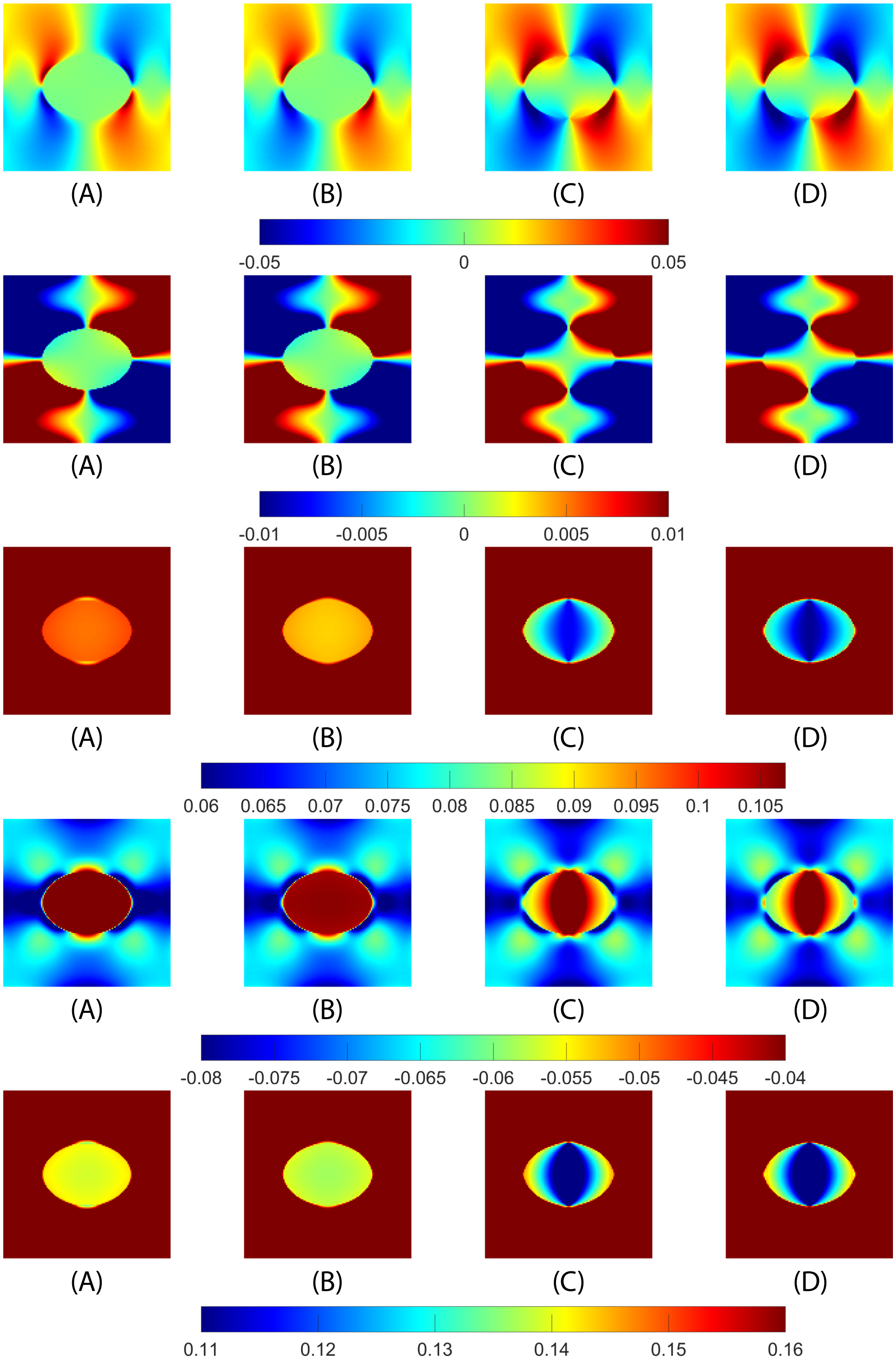

Figure 4.8: Axial shear strain, radial shear strain, first principal strain, second principal strain, and Von Mises strain at time points of 57.6 s (steady state) for samples A, B, C and D with elliptical shape, respectively.

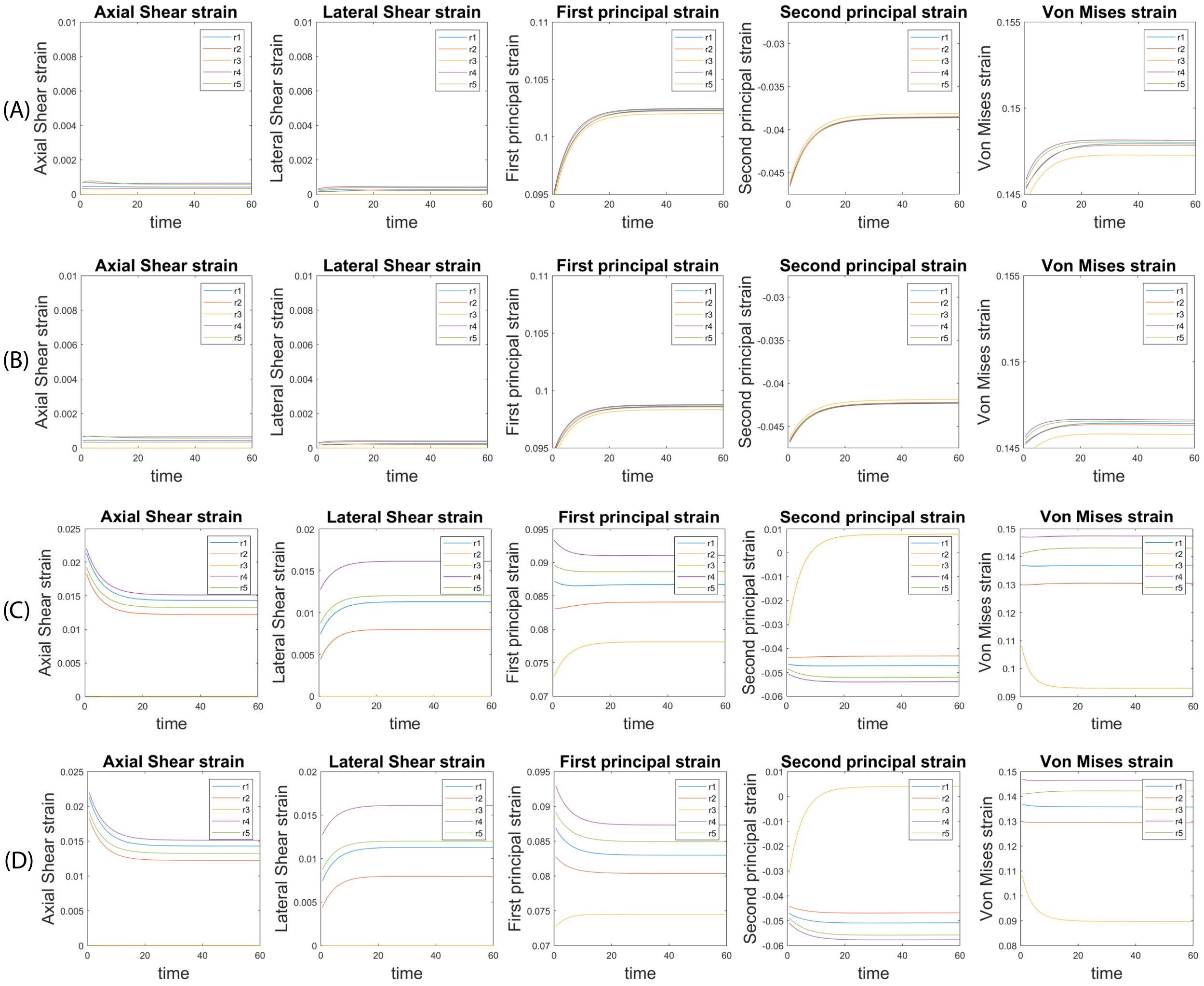

Figure 4.9: Time profiles of absolute axial and radial shear strains, first and second principal strains, and Von Mises strain at various locations inside cancers for samples A-D respectively.

4.1.2 Ultrasound Simulation

Axial and radial shear strains, first and second principal strains, and Von-Misses strain for sample D from ultrasound simulations with single realization are shown in Figs. 4.10. We can see that the ultrasound simulation results are consistent with the ideal case results, with the radial shear strain being much nosier inside and outside the inclusion. Although the result for the second principal strain is somewhat different from the FEM result outside the inclusion, the conclusion made from ideal cases in the central region remains valid. Other estimated strains for both cases match well with the corresponding strains obtained from FE simulations. The strain images clearly show the shape of cancer, so there is no need for more realizations. The simulated ultrasound system resembled the results from FEM. Therefore, the conclusions drawn from the previously discussed FE simulation results should be equally applicable to the ultrasound elastography simulations results and, possibly, future experimental results.

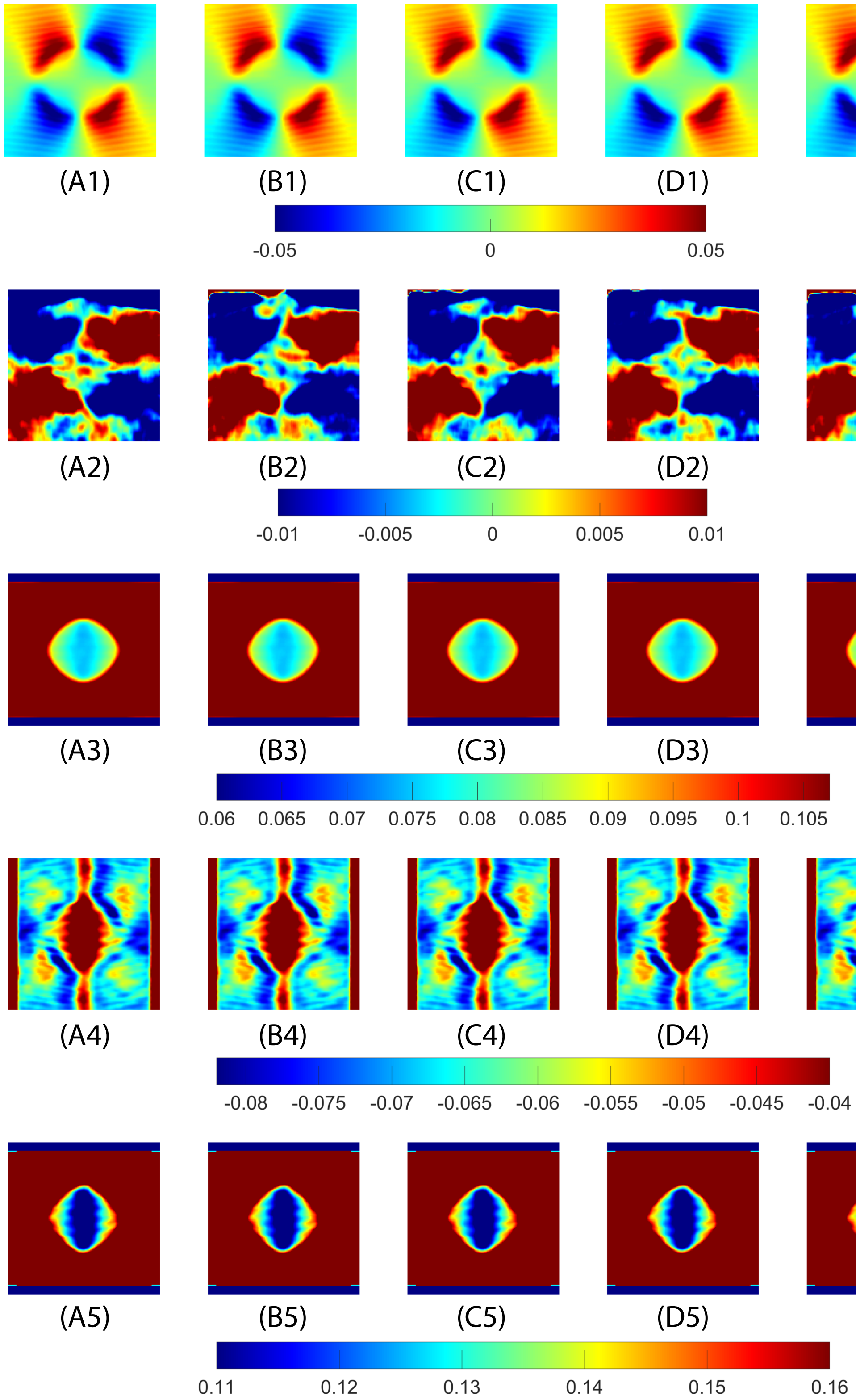

Figure 4.10: Axial and radial shear strains, first and second principal strains, Von Mises strain at time points of 0.6 s (0^+ s), 4.8 s, 9 s, 18 s and 57.6 s for samples D are shown in (A1-A5), (B1-B5), (C1-C5),(D1-D5) and (E1-E5), respectively. These strains are obtained from a single ultrasound simulation realization.

4.1.3 Animal Cancer Study

Previously acquired experiment data from animal cancers were analyzed to corroborate the simulation results. The in vivo data includes 118 frames of the untreated mice data pre-processed by DPHS methods for two or three consecutive weeks. The last frame (118th) of each strain matrix represents the steady-state. A GUI app is constructed to better display the data as strain imaging by using the MATLAB app designer feature, which is displayed in Fig. 4.11. The app displays B-mode imaging and all the strains that were analyzed in this study at each frame. Strain imaging can be analyzed frame by frame with more flexibility. All the strain images are resized to 128 * 128 pixels. Users can adjust the imaging displayed dynamic range for all strain images by using sliders or entering the value directly. Both the strain between successive frames and cumulative strain were analyzed. The "Strain Frame" option allows switching from individual successive strain frames to cumulative strain frames. Tumors can be manually segmented or using morphological operations by the "Tumor detection" function.

Fig. 4.12 to Fig. 4.16 provides grey scale B-mode and strains imaging of the tumor cell across untreated mice in vivo at different time points. We had data for three consecutive weeks for some tumors, while for others, we had data for only two consecutive weeks. Due to observation, M324, M326, and M14 are the top three cases where the strain images indicate a discernable appearance. M347 displayed in the appendix is the worst-case scenario, which demonstrates the failure of the application of strain imaging and how in-vivo strain imaging may be impacted by other factors such as noise. As recognized in B-mode imaging, the tumor is growing over time, and we can see that the tumors have approximately elliptical shapes and are oriented in the lateral direction. According to Kumm et al. [101] and Barr et al. [102], cancers frequently seem to be smaller on sonograms than on equivalent elastograms, while benign tumors seem to be the same size because the acicular spines that spread from the tumor or peripheral proliferative areas are challenging to detect on the B-mode image.

In the case of the in vivo data, there are complex boundary conditions and low signal-to-noise ratio due to attenuation and other effects. However, we did not observe axial shear strain inside

Figure 4.11: MATLAB GUI for in-vivo data.

the cancers in most cases. The lateral shear strain is very noisy and was not used to analyze the in vivo data. The first principal strain results appear to confirm what we observed from FEM with a lower strain value inside. For the second principal strain, the value is highest near the center of the inclusion and decreases near the boundary. Qualitatively, we could observe a gradient in Von Mises in most of the cases.

It is impossible to directly compare the results of simulations and experiments under the same condition because the mechanical properties, like young's modulus or Poisson's ratio, are unknown for the in-vivo data. In addition, boundary conditions and noise conditions are different. However, we can use the in vivo data to qualitatively and loosely validate the trends observed in the simulations results.

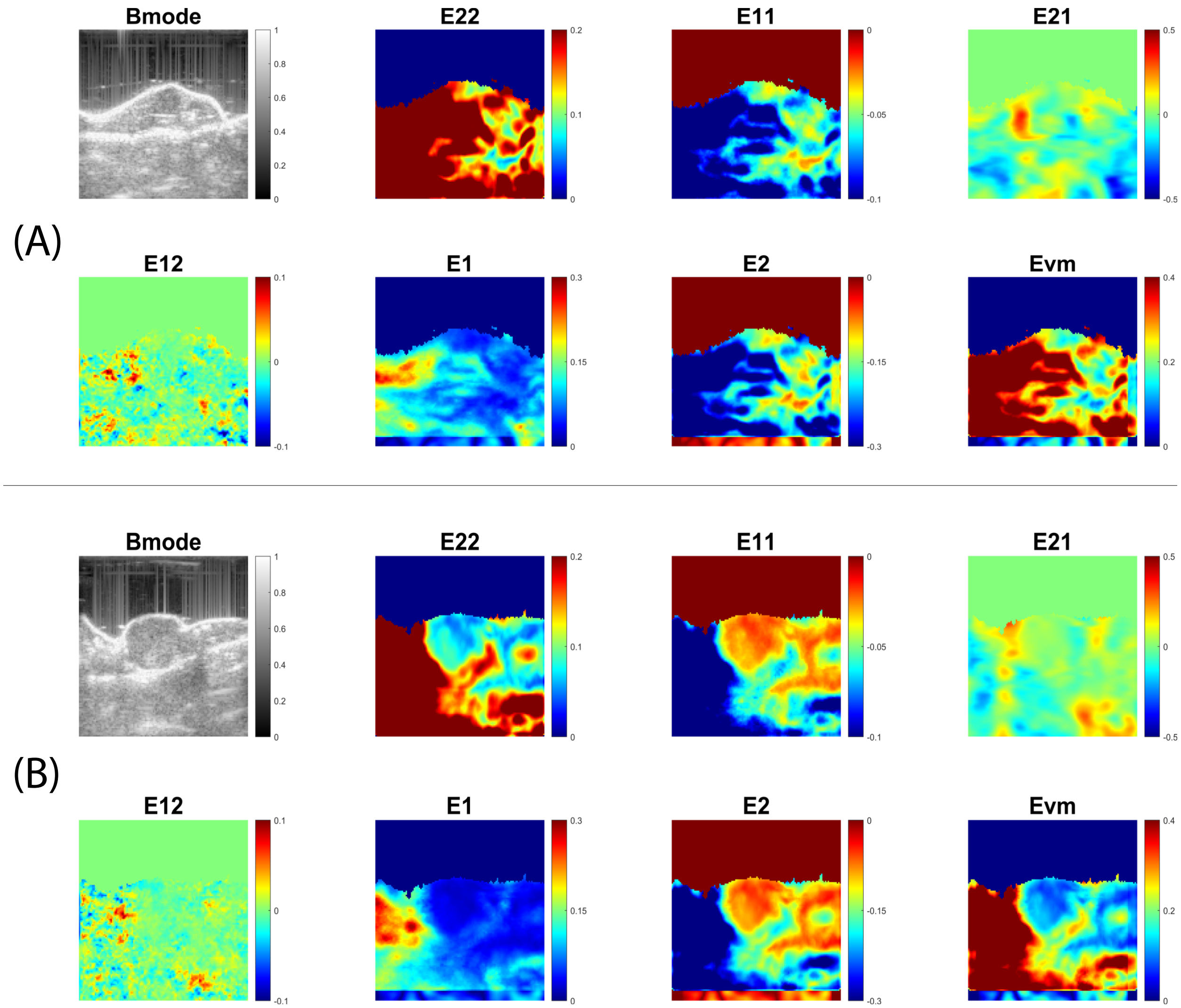

Figure 4.12: Bmode, axial strain (E22), radial strain (E11), axial shear strain (E12), radial shear strain (E21), first principal strain (E1), second principal strain (E2), Von Mises strain (Evm) for Mice data with label M324 in (A) Week 2 and (B) Week 3.

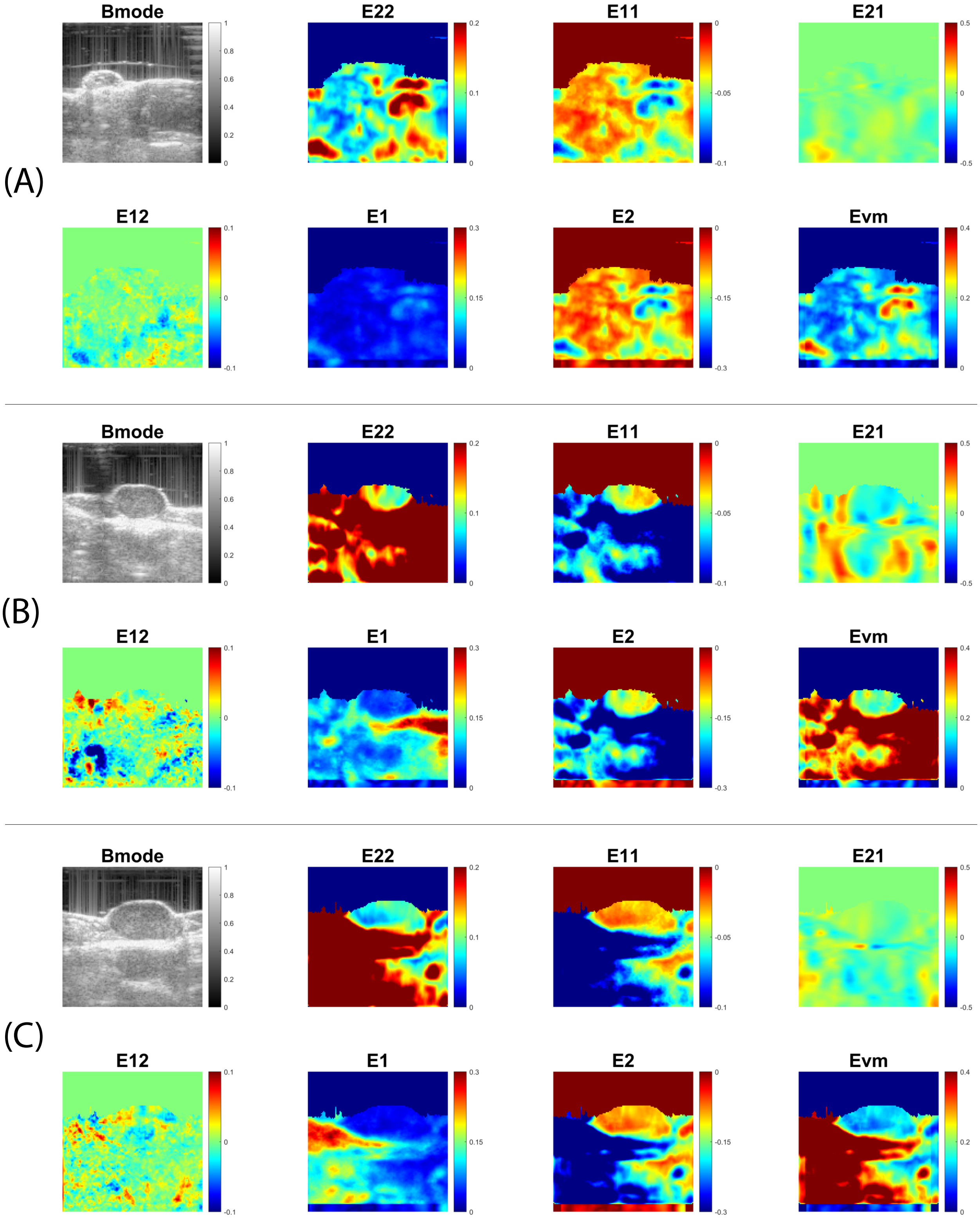

Figure 4.13: Bmode, axial strain (E22), radial strain (E11), axial shear strain (E12), radial shear strain (E21), first principal strain (E1), second principal strain (E2), Von Mises strain (Evm) for Mice data with label M326 in (A) Week 1 (B) Week 2 and (C) Week 3.

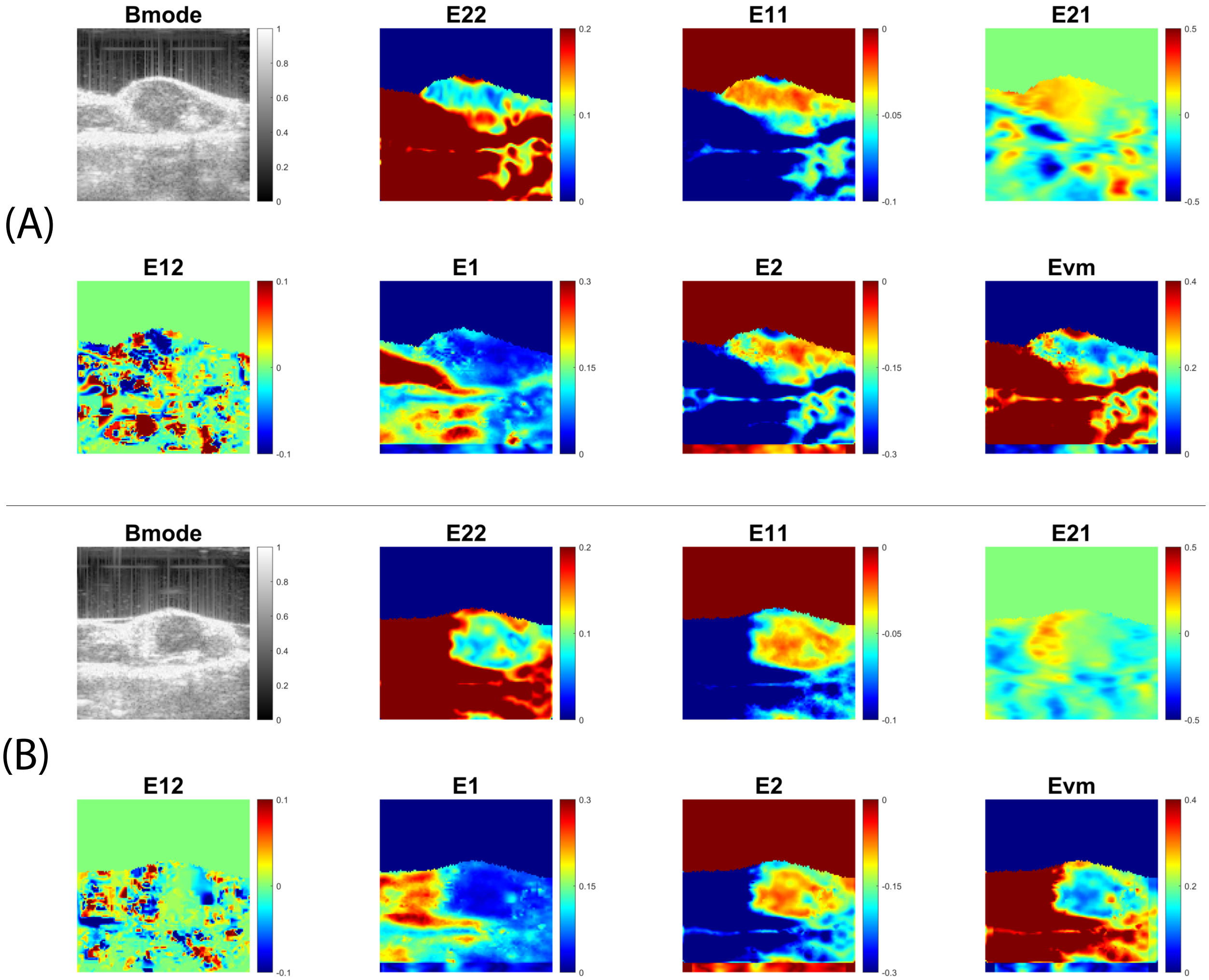

Figure 4.14: Bmode, axial strain (E22), radial strain (E11), axial shear strain (E12), radial shear strain (E21), first principal strain (E1), second principal strain (E2), Von Mises strain (Evm) for Mice data with label M14 in (A) Week 2 and (B) Week 3.

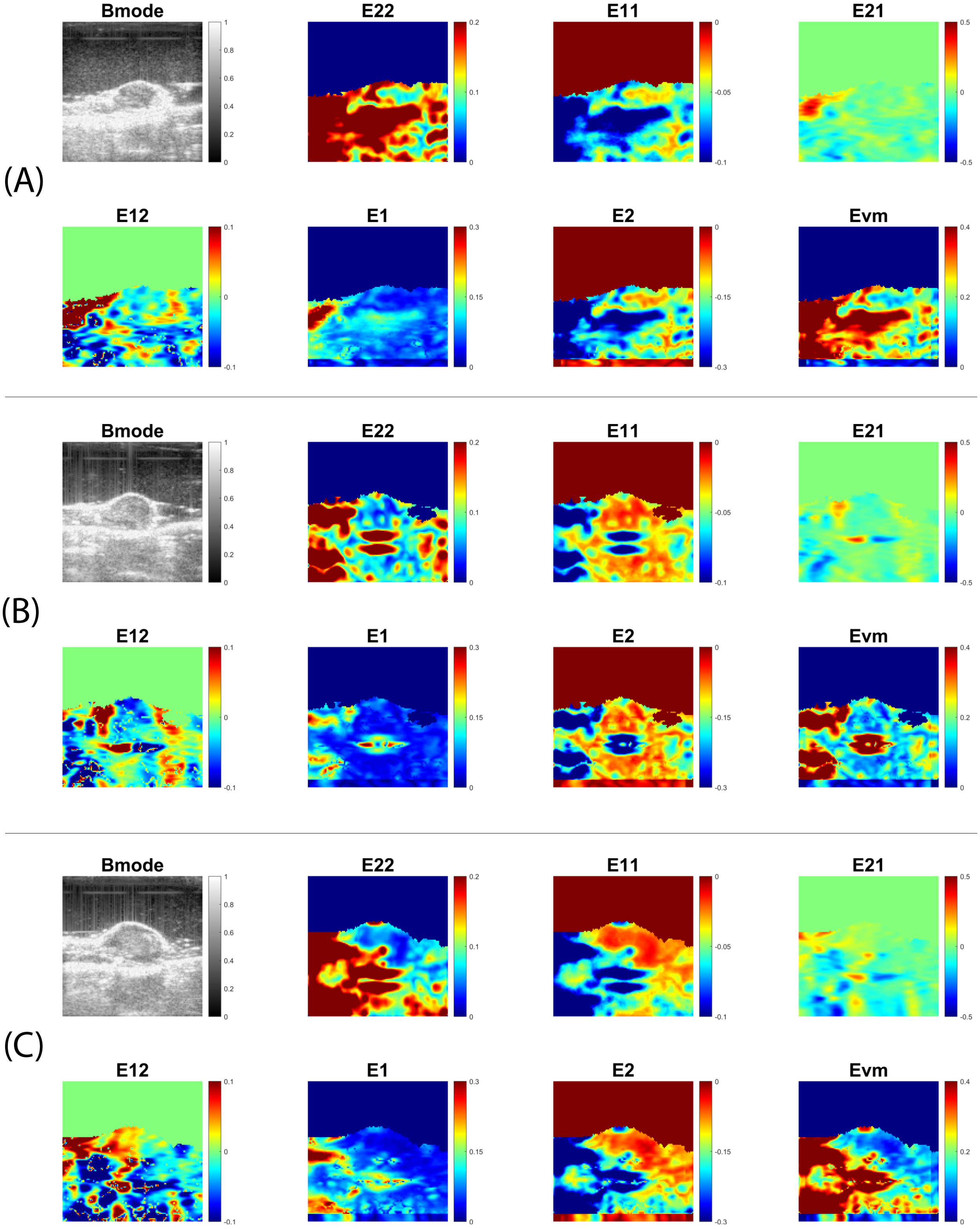

Figure 4.15: Bmode, axial strain (E22), radial strain (E11), axial shear strain (E12), radial shear strain (E21), first principal strain (E1), second principal strain (E2), Von Mises strain (Evm) for Mice data with label M24 in (A) Week 2 and (B) Week 3.

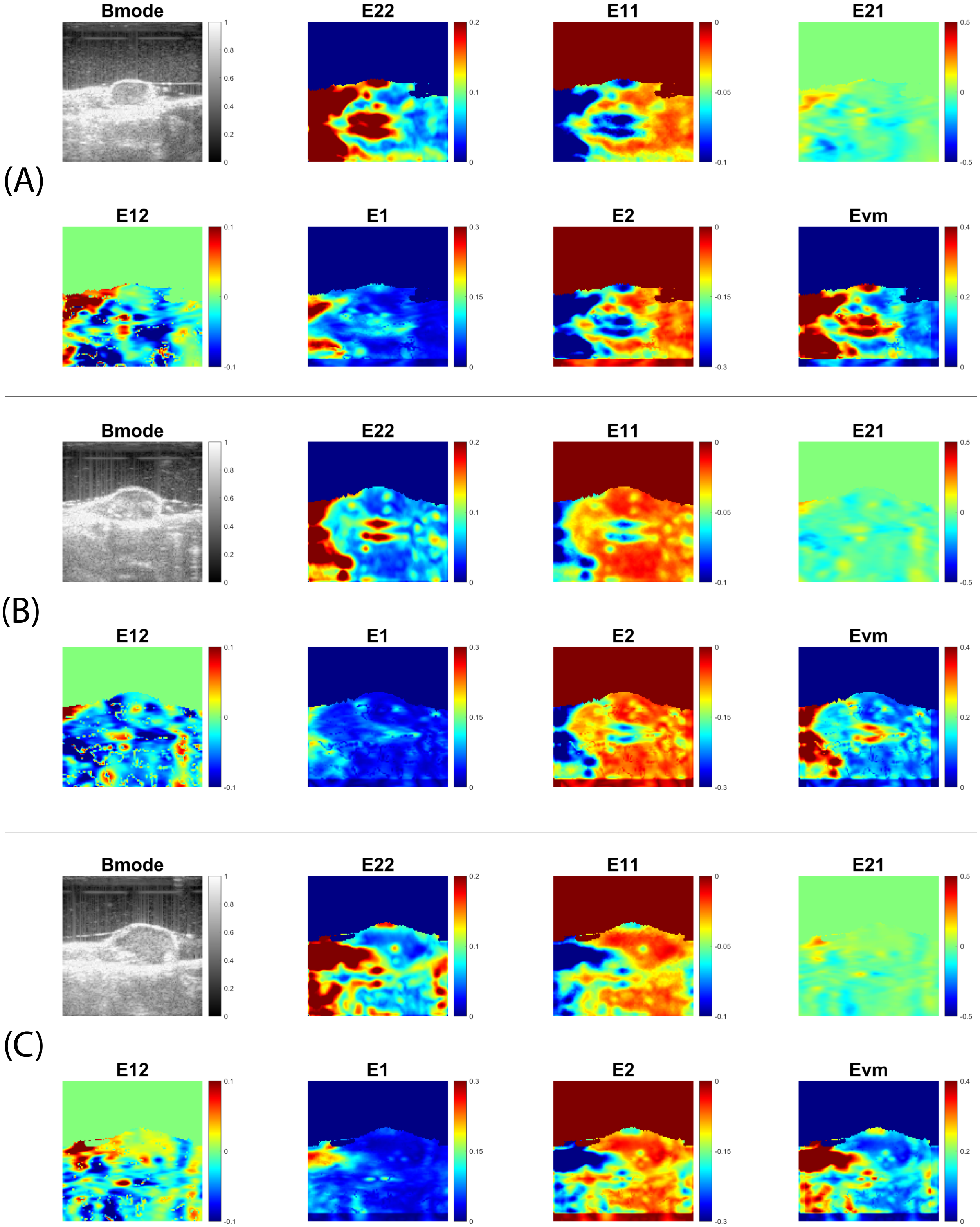

Figure 4.16: Bmode, axial strain (E22), radial strain (E11), axial shear strain (E12), radial shear strain (E21), first principal strain (E1), second principal strain (E2), Von Mises strain (Evm) for Mice data with label M5 in (A) Week 2 and (B) Week 3.

4.2 Benign Tumor Simulation Analysis

Benign tumors with different friction at steady state are shown in Fig. 4.19 - Fig. 4.23. We could observe that as the friction increases, the result will be closer to malignant tumors. The axial shear strain and the radial shear strain have decreased inside the inclusion from friction 0.01 to friction 10. The center will always remain nearly zero shear strain. There exists a changing polarity inside the inclusion. For the first principal strain, the strain decreases in the center and increases at the peripheral. We could observe slight changes with the presence of IFP and more obvious changes with the presence of SS for the second principal strain. As for the Von Mises strain, the part along the axial direction has a decreasing strain, and the rest has an increasing strain. The main observation is that it is harder to identify the strain pattern for shear strains and second principal strains with low friction values. This phenomenon means that mobility will influence the shear strains and the second principal strains. While the malignant tumor reached a steady state within acceptable clinical time, it took a long time for the benign tumor to reach a steady state. The long-time constant adds some uncertainly for the appearance of friction.

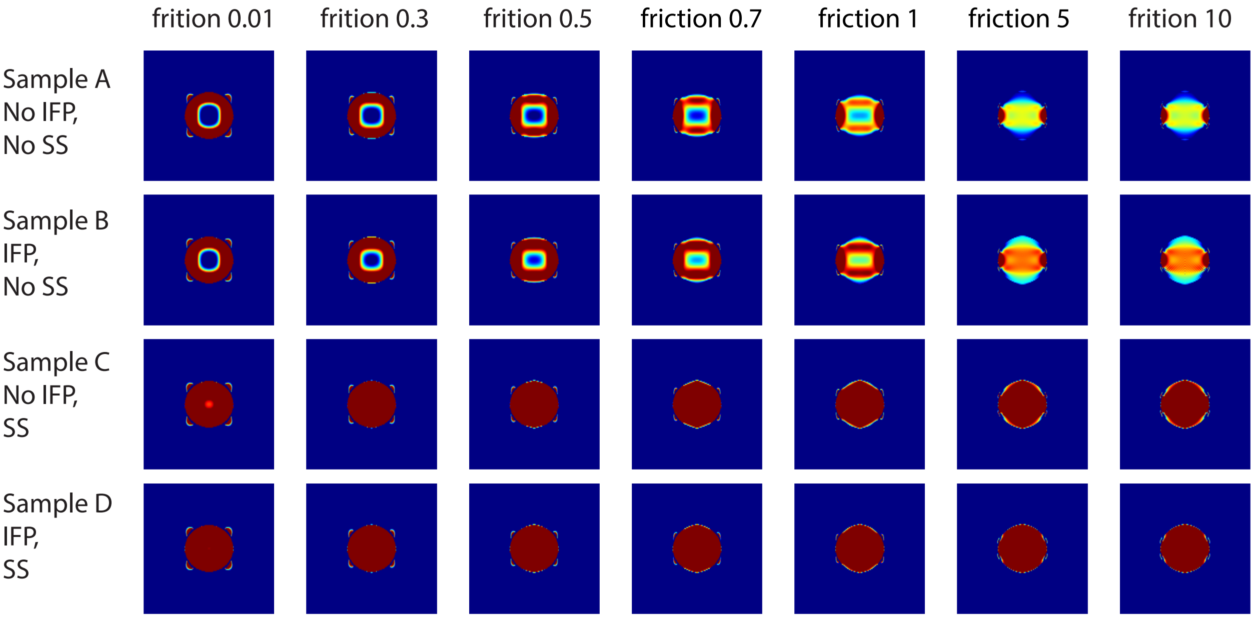

Figure 4.17: Axial strain for Benign tumor with friction for samples A-D.

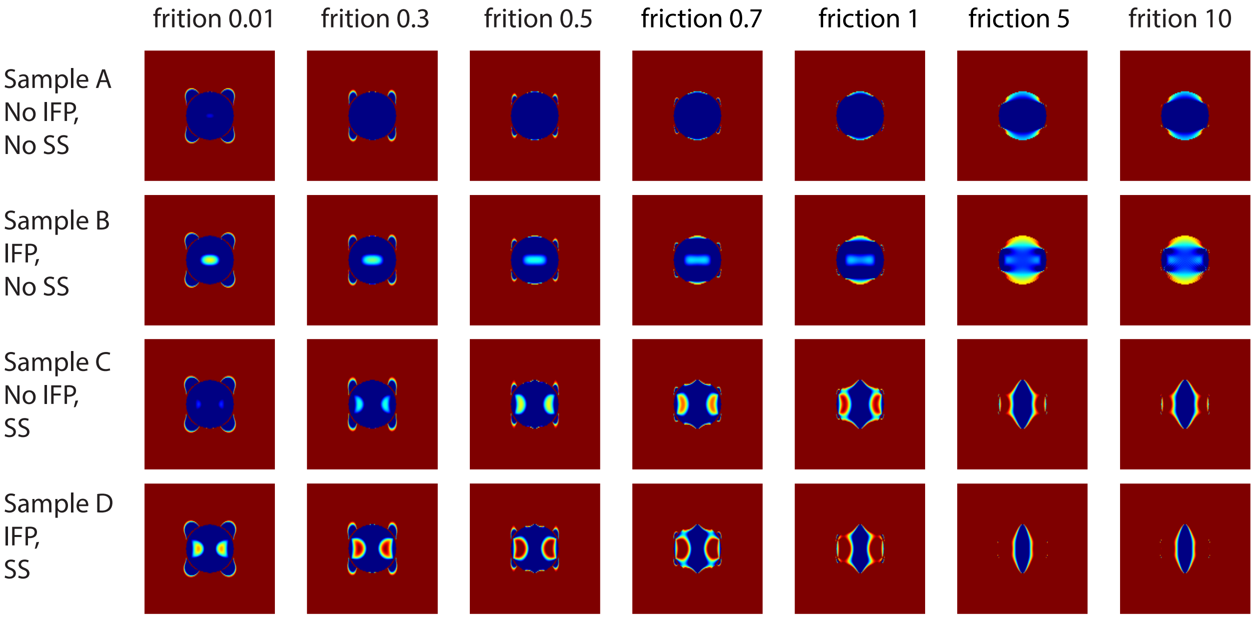

Figure 4.18: Radial strain for Benign tumor with friction for samples A-D.

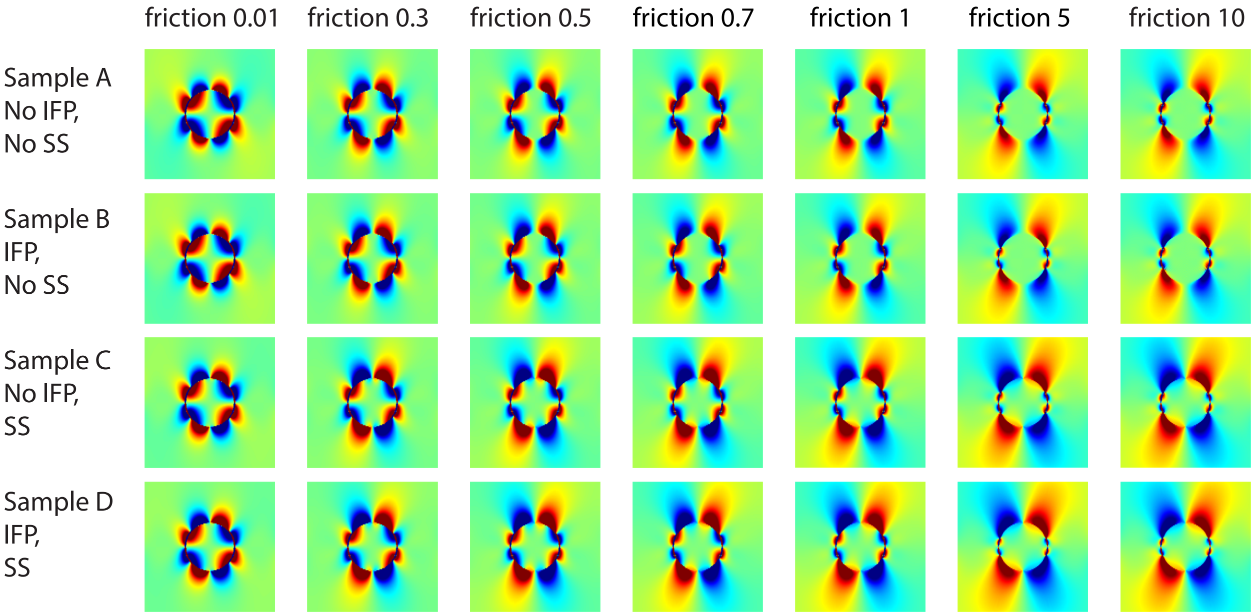

Figure 4.19: Axial shear strain for Benign tumor with friction for samples A-D.

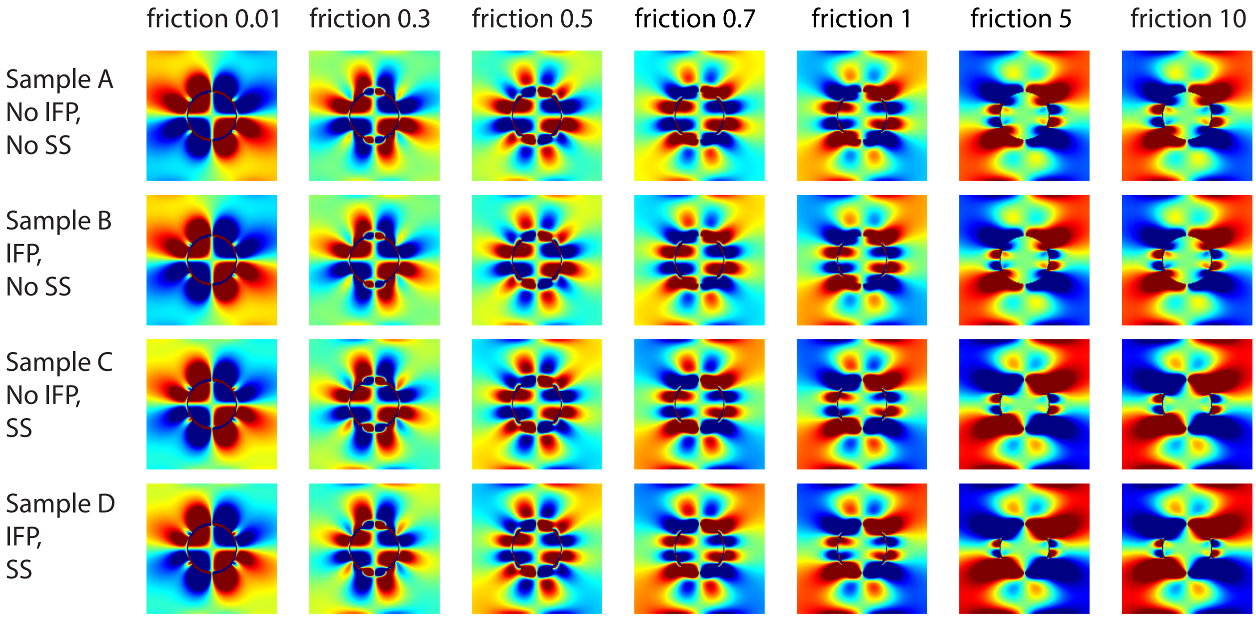

Figure 4.20: Radial shear strain for Benign tumor with friction for samples A-D.

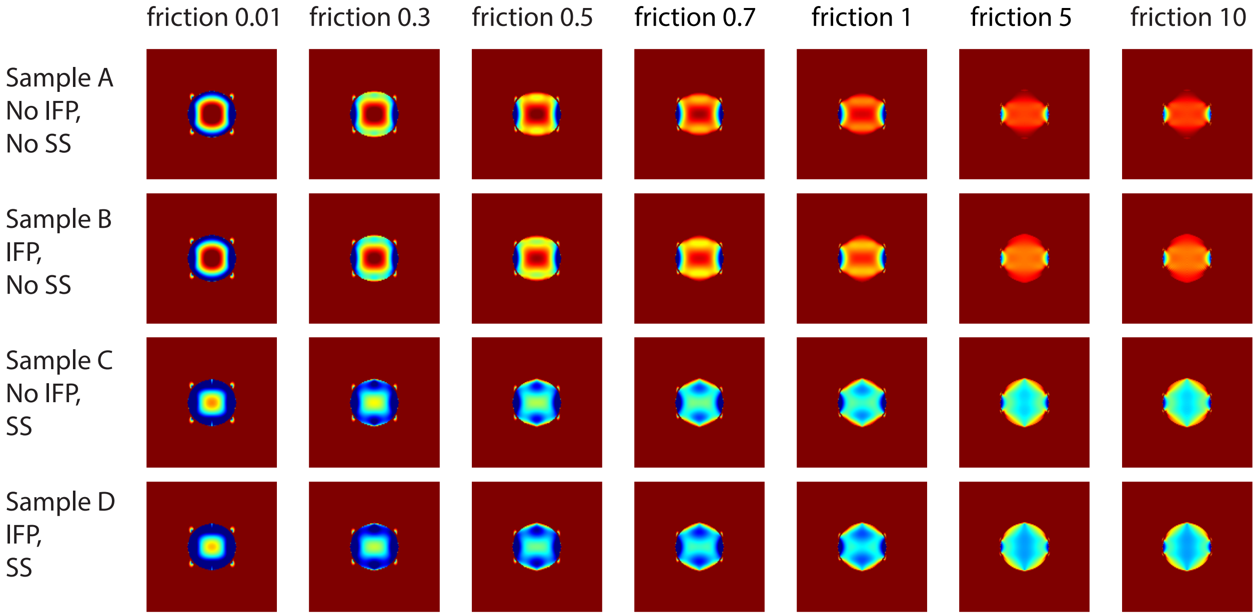

Figure 4.21: First principal strain for Benign tumor with friction for samples A-D.

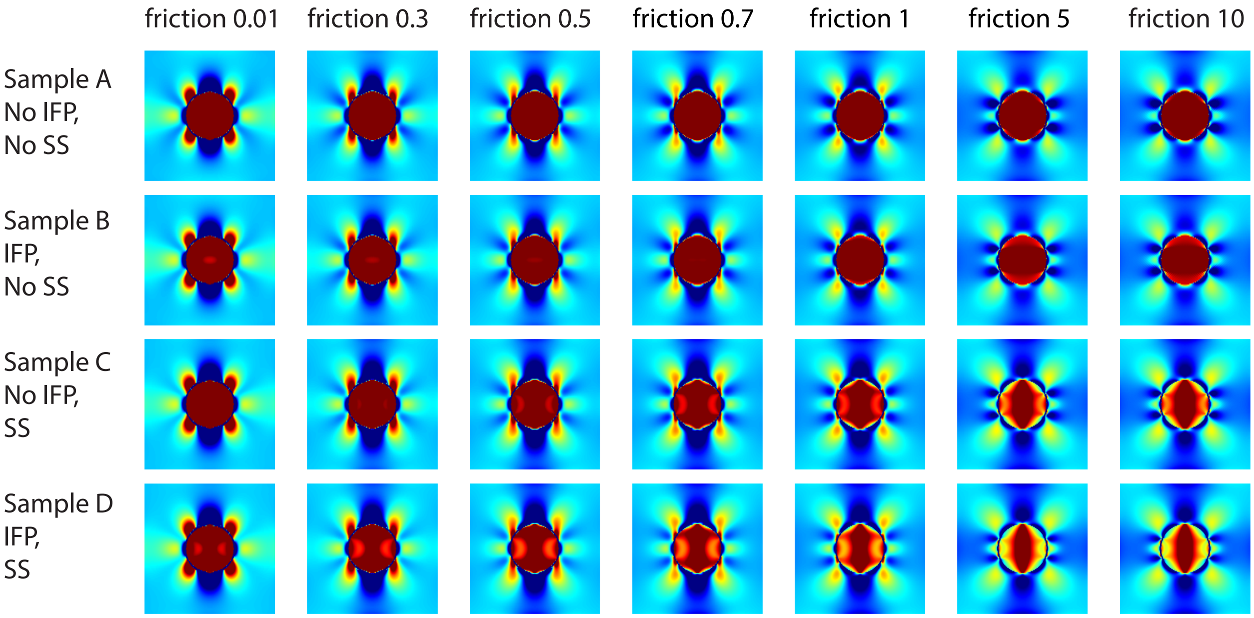

Figure 4.22: Second principal strain for Benign tumor with friction for samples A-D.

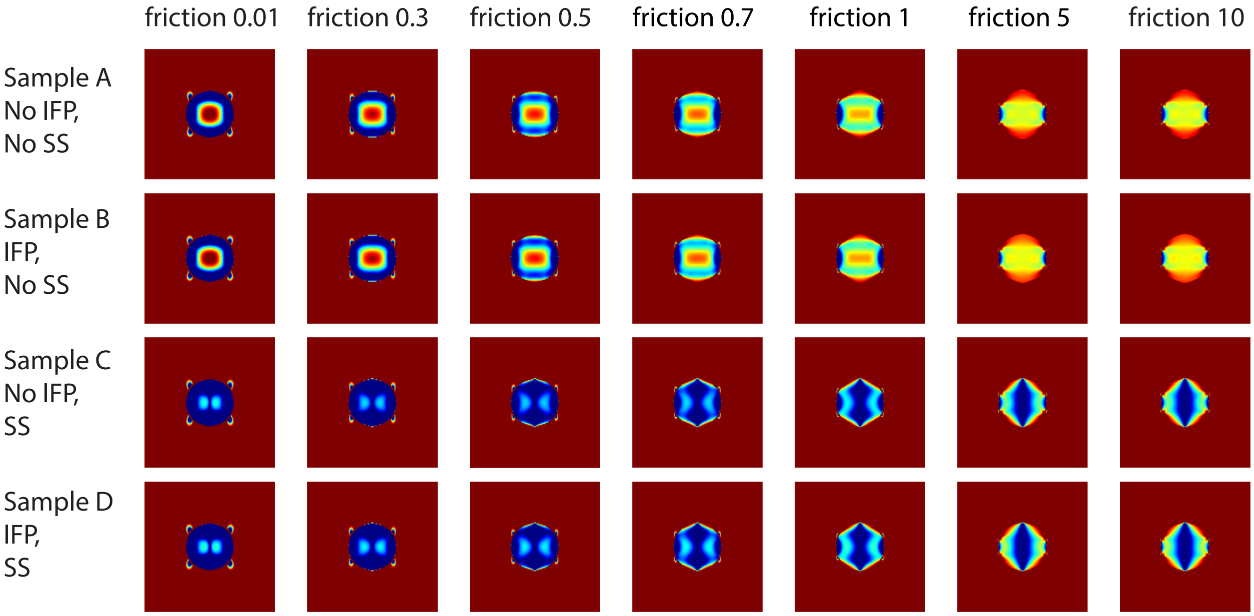

Figure 4.23: Von Mises strain for Benign tumor with friction for samples A-D.

4.3 Statistical Analysis of FEM Simulation

In the inclusion, we conducted statistical analysis on the axial shear, first principal, and Von Mises strains. As observed in the ultrasound simulations and in-vivo data, the radial shear strain and the second principal strain might be significantly affected by noise. Thus, radial strain and second principal strain were excluded for statistical analysis. The results from statistical analysis, which includes x-y plots, normal quantile plots, histograms, means and standard deviation, and nonparametric comparison, are shown in Fig. 4.24 - Fig. 4.26. We could observe that the strains inside the inclusion do not follow a normal distribution from the normal quantile plot, but there are many outliers. In that case, nonparametric studies should be performed. In this project, we selected the Wilcoxon method for nonparametric comparisons for each pair. When comparing paired data, the Wilcoxon technique is used as an alternative to the paired Student's t-test. The hypothesis is that the results are not statistically different with 95% confidence level. We noticed that all the p-values for axial shear strain inside the inclusion are greater than 5%. Thus, we conclude that the changes of axial shear strain inside the inclusion due to IFP and SS are not statistically significant. The first principal strain indicates a statistical difference with the presence of IFP and SS. The first principal strain is sensitive to both the presence of IFP and SS. This is also true for the Von Mises strain, except that the case for SS only and IFP and SS are not statistically significant. That means that the Von Mises strain is sensitive to SS more than IFP.

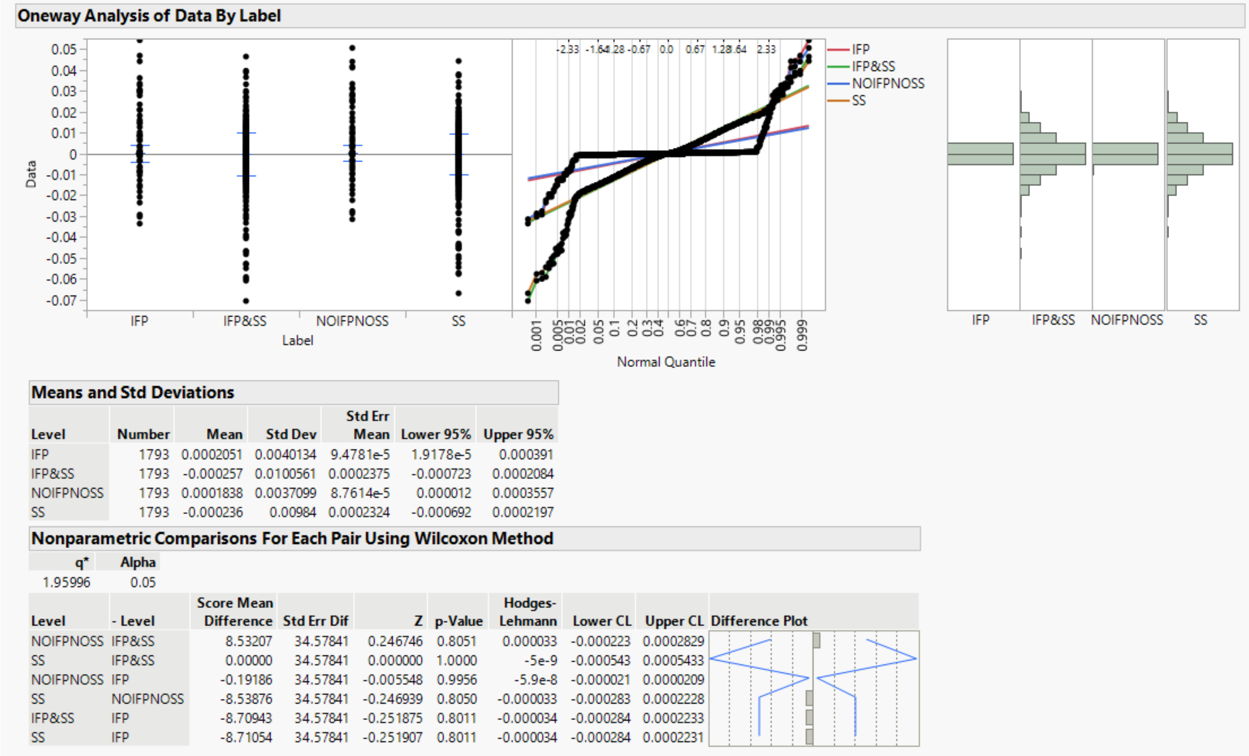

Oneway Analysis of Data By Label

Means and Std Deviations

Level	Number	Mean	Std Dev	Std Err Mean	Lower 95%	Upper 95%
IFP	1793	0.0002051	0.0040134	9.4781e-5	1.9178e-5	0.000391
IFP&SS	1793	-0.000257	0.0100561	0.0002375	-0.000723	0.0002084
NOIFPNOSS	1793	0.0001838	0.0037099	8.7614e-5	0.000012	0.0003557
SS	1793	-0.000236	0.00984	0.0002324	-0.000692	0.0002197

Nonparametric Comparisons For Each Pair Using Wilcoxon Method

q*	Alpha
1.95996	0.05

Level	- Level	Score Mean Difference	Std Err Dif	Z	p-Value	Hodges-Lehmann	Lower CL	Upper CL	Difference Plot
NOIFPNOSS	IFP&SS	8.53207	34.57841	0.246746	0.8051	0.000033	-0.000223	0.0002829	
SS	IFP&SS	0.00000	34.57841	0.000000	1.0000	-5e-9	-0.000543	0.0005433	
NOIFPNOSS	IFP	-0.19186	34.57841	-0.005548	0.9956	-5.9e-8	-0.000021	0.0000209	
SS	NOIFPNOSS	-8.53876	34.57841	-0.246939	0.8050	-0.000033	-0.000283	0.0002228	
IFP&SS	IFP	-8.70943	34.57841	-0.251875	0.8011	-0.000034	-0.000284	0.0002233	
SS	IFP	-8.71054	34.57841	-0.251907	0.8011	-0.000034	-0.000284	0.0002231	

Figure 4.24: Statistical analysis of the axial shear strain within the cancer for simulated samples A-D.

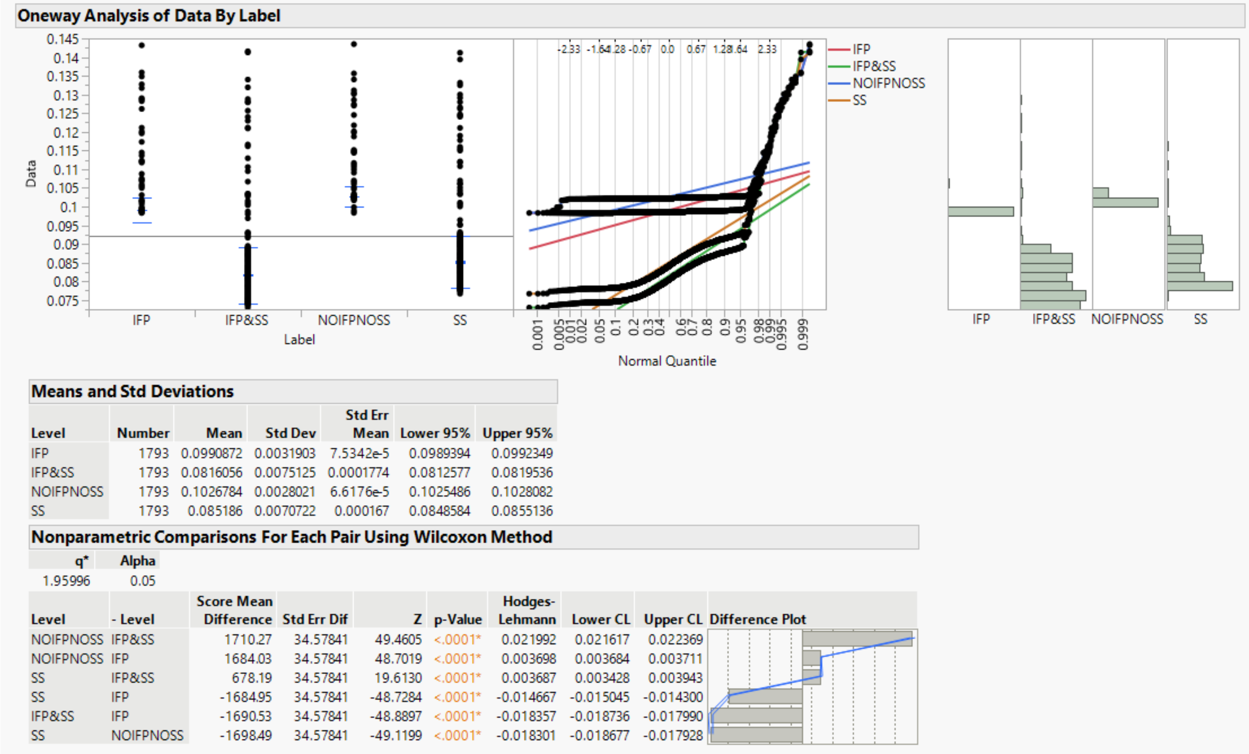

Oneway Analysis of Data By Label

Means and Std Deviations

Level	Number	Mean	Std Dev	Std Err Mean	Lower 95%	Upper 95%
IFP	1793	0.0990872	0.0031903	7.5342e-5	0.0989394	0.0992349
IFP&SS	1793	0.0816056	0.0075125	0.0001774	0.0812577	0.0819536
NOIFPNOSS	1793	0.1026784	0.0028021	6.6176e-5	0.1025486	0.1028082
SS	1793	0.085186	0.0070722	0.000167	0.0848584	0.0855136

Nonparametric Comparisons For Each Pair Using Wilcoxon Method

q*	Alpha
1.95996	0.05

Level	- Level	Score Mean Difference	Std Err Dif	Z	p-Value	Hodges-Lehmann	Lower CL	Upper CL	Difference Plot
NOIFPNOSS	IFP&SS	1710.27	34.57841	49.4605	<.0001*	0.021992	0.021617	0.022369	
NOIFPNOSS	IFP	1684.03	34.57841	48.7019	<.0001*	0.003698	0.003684	0.003711	
SS	IFP&SS	678.19	34.57841	19.6130	<.0001*	0.003687	0.003428	0.003943	
SS	IFP	-1684.95	34.57841	-48.7284	<.0001*	-0.014667	-0.015045	-0.014300	
IFP&SS	IFP	-1690.53	34.57841	-48.8897	<.0001*	-0.018357	-0.018736	-0.017990	
SS	NOIFPNOSS	-1698.49	34.57841	-49.1199	<.0001*	-0.018301	-0.018677	-0.017928	

Figure 4.25: Statistical analysis of the first principal strain within the cancer for simulated samples A-D.

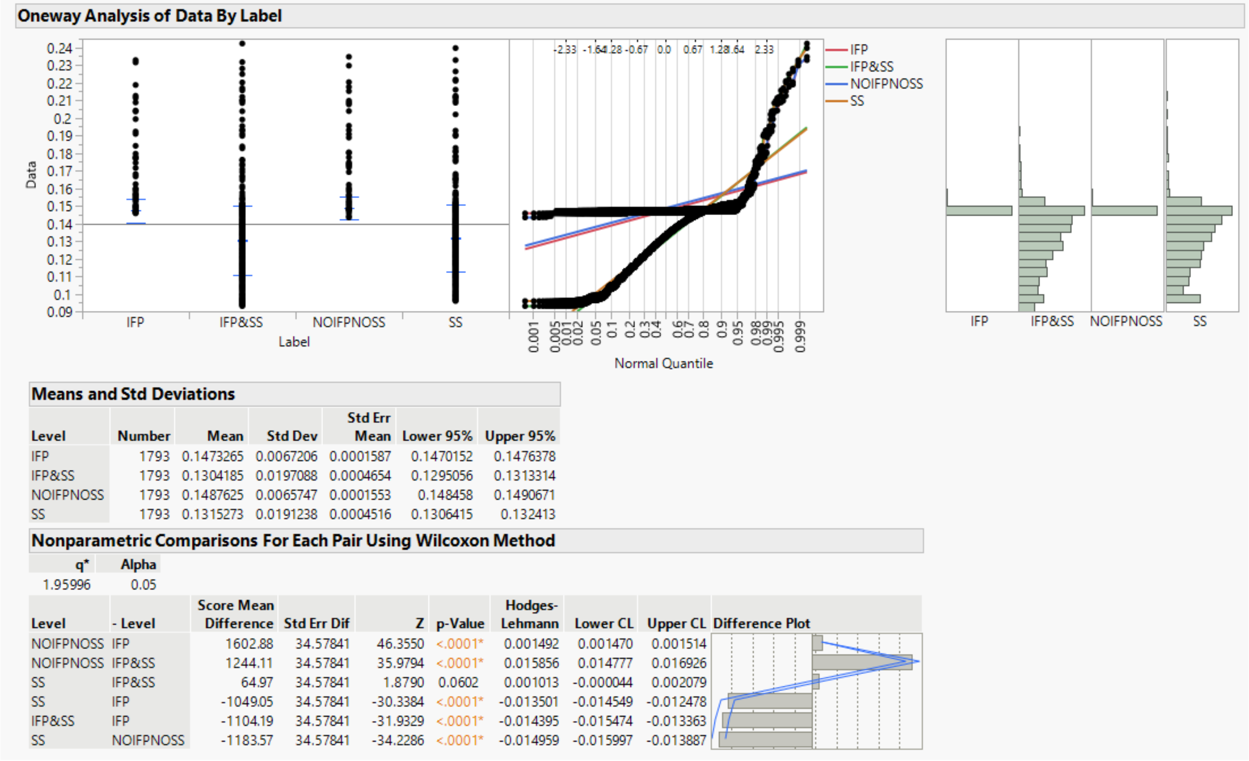

Oneway Analysis of Data By Label

Means and Std Deviations

Level	Number	Mean	Std Dev	Std Err Mean	Lower 95%	Upper 95%
IFP	1793	0.1473265	0.0067206	0.0001587	0.1470152	0.1476378
IFP&SS	1793	0.1304185	0.0197088	0.0004654	0.1295056	0.1313314
NOIFPNOSS	1793	0.1487625	0.0065747	0.0001553	0.148458	0.1490671
SS	1793	0.1315273	0.0191238	0.0004516	0.1306415	0.132413

Nonparametric Comparisons For Each Pair Using Wilcoxon Method

q*	Alpha
1.95996	0.05

Level	- Level	Score Mean Difference	Std Err Dif	Z	p-Value	Hodges-Lehmann	Lower CL	Upper CL	Difference Plot
NOIFPNOSS	IFP	1602.88	34.57841	46.3550	<.0001*	0.001492	0.001470	0.001514	
NOIFPNOSS	IFP&SS	1244.11	34.57841	35.9794	<.0001*	0.015856	0.014777	0.016926	
SS	IFP&SS	64.97	34.57841	1.8790	0.0602	0.001013	-0.000044	0.002079	
SS	IFP	-1049.05	34.57841	-30.3384	<.0001*	-0.013501	-0.014549	-0.012478	
IFP&SS	IFP	-1104.19	34.57841	-31.9329	<.0001*	-0.014395	-0.015474	-0.013363	
SS	NOIFPNOSS	-1183.57	34.57841	-34.2286	<.0001*	-0.014959	-0.015997	-0.013887	

Figure 4.26: Statistical analysis of the Von Mises strain within the cancer for simulated samples A-D.

4.4 Discussion

In this work, we have closely examined the change of shear and derived strains in response to the presence of IFP and SS for cancers under compression. IFP and SS are of clinical importance but are exceedingly difficult to be assessed non-invasively. With additional strain, we may gain additional information about IFP and SS. Thus, we suggested Von mises strain as a potential elastographic marker and evaluated it using FEM, ultrasound simulation, and in-vivo data. Although prior work has noted that Von Mises elastography may play an essential role in tumor classification, it has not investigated the link of the Von Mises with the presence of IFP and SS. Poroelastography is a qualitative method to differentiate a tumor from normal tissue. Most observations in this project come from the FEM simulations, the results of which are considered as the ideal cases. The simulation may benefit from IFP and SS incorporation compared to the traditional ultrasound elastography when interpreting the elastographic results because it is more realistic.

A previous study of our group explored the changes of axial and radial normal strains, volumetric strains, and fluid pressure with IFP and SS. In that study, axial strain increases with the presence of IFP and SS. The radial strain increases with the presence of IFP and increases strain on the peripheral with the presence of SS. The results in this study confirmed that the normal strains are associated with the IFP and SS by using different inputs. One of the aims of this study was to extend the previous study. The shear, principal, and Von Mises strains were investigated, adding broadness and novelty to this study.

In summary, one significant finding of this study is that the first principal and the Von Mises could be considered as sensitive markers to the presence of IFP and SS. The presence of IFP causes a reduction of the first principal strain and the Von Mises strain inside the tumor at the steady-state. The first principal strain is more spatially uniform inside inclusion. In the presence of SS, the principal strain and Von Mises strain become space-varying inside the inclusion, and the central part of the tumor behaves like a more compressible material than the periphery part of the tumor. The elliptical tumor with zero orientation corroborates the findings of the spherical tumor. However, we could still see slight changes due to geometry. Therefore, more changes might occur with irregularly shaped tumors. Up to now, it is still too early to claim the first principal strain and the Von Mises strain as biomarkers. More in-vivo studies have to be done.

Another finding suggests that although the FEM indicated that axial shear strain, radial shear strain, and the second principal strain have the potential to become a marker, it does not provide helpful information to make a classification in real cases. The radial strain and the second principal strain were not that noisy resistant compared to other strains. The theory behind the phenomenon is that radial shear strain is along the lateral direction, and the second principal strain is closer to the lateral direction. The image resolution in the lateral direction is very bad. The shear strains and the second principal strain contain information outside the tumor with negative and positive strain values, which results in ambiguous and difficult-to-interpret imaging. Additionally, shear strains are greatly influenced by the mobility of the tumor. The identified pattern becomes harder to identify with increasing mobility.

In accordance with the FEM simulation, the results from the in-vivo mice have demonstrated that the feasibility of using the derived strains. Five out of six imagings have surprisingly good quality. The results loosely prove that it is possible to generate the strains in practice.

The dynamic range of a poroelastogram is essential in providing appropriate visualization of the region of interest. In this study, we manually adjusted the dynamic range for FEM and in-vivo data. For FEM, the dynamic range is determined by the statistics of the pixel intensity. In contrast, the dynamic range for the in-vivo data is selected by using the pixels close to the lesion boundary. The elastography plot for benign tumor at steady-state had the same dynamic range as the malignant tumor in the purpose of comparison.

5. CONCLUSIONS AND FUTURE WORK

This research involved the development of finite element models and the generation of strain poroelastograms. The influence of different structural and material properties on measured strains was examined. This study also included the generation of the very first experimental Von Mises elastogram of in-vivo cancers. Moreover, the effect of SS and IFP on the shear and derived strains generated in an inclusion during a poroelastography experiment was investigated. Our study suggests that a non-zero IFP inside the inclusion does not create any shear strain, while non-zero SS creates visible shear strains inside the inclusion. Radial shear strain is too noisy to be used in practice, as demonstrated by the ultrasonic and in-vivo results. In contrast, the axial shear strain is more robust. However, the axial shear strain alone may not be a good marker for IFP and SS because friction also causes changes of shear strains inside the inclusion, although a change in polarity may aid in making the difference from the no friction case. In addition, the changes identified from ideal cases are not statistically significant. We have shown that the features from the first principal strain and Von Mises strain elastograms may be more robust indicators of the presence of SS. Noise also influences the second principal strain. Hence, the second principal strain is not of primary choice as a potential marker. Furthermore, the principal strains and the Von mises strain mark measurable changes with the presence of IFP, with the first principal being more sensitive to IFP than the Von Mises strain. The first principal strain and the Von Mises strain have the potential to be new elastographic markers in clinical applications.

5.1 Limitations

This study has several limitations. Firstly, the outcome relies heavily on the simulations. While constructing the simulation models, there are various assumptions, and some of those assumptions may not hold true in practice. From an operational perspective, the amount and the direction of the pressure applied by the examiner will affect the results. Moreover, the tumor was assumed to be poroelastic with a linear elastic solid phase. This assumption is frequently used in experiments related to the mechanical behavior of tissues. However, this assumption may result in an oversimplification of clinical conditions. Secondly, the in-vivo data should be interpreted as proof-of-principle of feasibility and not a complete validation study. Additional cases are required to check the effect of acquisition strains. Moreover, the equipment and protocol may not be optimized for our specific project. Lastly, we did not consider the impact of lymphatic permeability on tumor mechanical activity. Although lymphatic permeability is marginal in comparison to vascular permeability, according to published data, it may not be ignored. Despite its limitations, this study adds to our understanding of how the presence of IFP and SS affects the strain poroelastograms and the prospect of novel methods for assessing the two parameters.

5.2 Future Study

Improving Model Complexity

In this project, FE simulations were carried out using a simplified model that integrated linearly elastic materials with biphasic theory with a specified shape and simple boundary conditions. The simplified model might not be sufficient to meet practical conditions. A more complex simulation that enables reliable modeling of the strain changes occurring in simulated media having similar proposed properties should be developed and evaluated independently.

In terms of future work, it would be engaging in expanding the current bi-phasic model into a multi-phase and multi-component model. In that case, other commonly used poroelastic properties like viscosity and fluid saturation may be added to the current model. For the sake of simplicity, we assume that the tumor is spherical or elliptical. The tumor geometry could be changed to test the sensitivity of the work. The orientation of the tumor could also be investigated.

Furthermore, the investigation was limited to the application of uniaxial compression. The orientation of the applied load may be investigated as well. Additionally, multiple tumors might be discovered due to the nature of tumor progression and the appearance of metastatic tumors. A model with multiple tumors may be built to see how the presence of a new tumor will influence the current results.

Validation of Results

More data should be obtained in vivo to corroborate the theory, unify diagnostic criteria for the strains, and optimize elasticity parameter selection using updated acquisition systems.

New Method to Assess IFP and SS

In this project, we have identified sensitive markers of IFP and SS. The relationship between sensitive markers and IFP and SS should be further studied to find a new way to assess IFP and SS in cancers.

REFERENCES

[1] K. D. Kochanek, J. Xu, and E. Arias, "Mortality in the united states," 2020. Retrived From `https://www.cdc.gov/nchs/data/databriefs/db395-H.pdf`.

[2] CDC, "Basic information about breast cancer," 2021. Retrived From `https://www.cdc.gov/cancer/breast/basic_info/index.htm`.

[3] A. C. Society, "Breast cancer facts &figures 2019-2020," 2019. Retrived From `https://www.cancer.org/content/dam/cancer-org/research/cancer-facts-and-statistics/breast-cancer-facts-and-figures/breast-cancer-facts-and-figures-2019-2020.pdf`.

[4] E. Devolli-Disha, S. Manxhuka-Kërliu, H. Ymeri, and A. Kutllovci, "Comparative accuracy of mammography and ultrasound in women with breast symptoms according to age and breast density," *Bosnian Journal of Basic Medical Sciences*, vol. 9, no. 2, pp. 131–136, 2009.

[5] K. Marcomini, E. Fleury, V. Oliveira, A. Carneiro, H. Schiabel, and R. Nishikawa, "Evaluation of a computer-aided diagnosis system in the classification of lesions in breast strain elastography imaging," *Bioengineering*, vol. 5, no. 3, p. 62, 2018.

[6] K. E. Fry, "Benign lesions of the breast," *CA: A Cancer Journal for Clinicians*, vol. 4, no. 5, pp. 160–161, 1954.

[7] Q. Liu, Q. Luo, Y. Ju, and G. Song, "Role of the mechanical microenvironment in cancer development and progression," *Cancer Biology and Medicine*, vol. 17, no. 2, pp. 282–292, 2020.

[8] A. Itoh, E. Ueno, E. Tohno, H. Kamma, H. Takahashi, T. Shiina, M. Yamakawa, and T. Matsumura, "Breast disease: Clinical application of us elastography for diagnosis," *Radiology*, vol. 239, no. 2, pp. 341–350, 2006.

[9] J. Cohen, I. Riishede, J. F. Carlsen, T.-L. Lambine, M. S. Dam, M. M. Petersen, M. B. Nielsen, and C. Ewertsen, "Can strain elastography predict malignancy of soft tissue tumors

in a tertiary sarcoma center?," *Diagnostics*, vol. 10, no. 3, p. 148, 2020.

[10] S. Li, L. Liu, and G. Lv, "Diagnostic value of strain elastography for differentiating benign and malignant soft tissue masses," *Oncology Letters*, vol. 14, no. 2, pp. 2041–2044, 2017.

[11] J. M. Chang, J.-K. Won, K.-B. Lee, I. A. Park, A. Yi, and W. K. Moon, "Comparison of shear-wave and strain ultrasound elastography in the differentiation of benign and malignant breast lesions," *American Journal of Roentgenology*, vol. 201, no. 2, pp. W347–W356, 2013.

[12] J. Ophir, S. K. Alam, B. Garra, F. Kallel, E. Konofagou, T. Krouskop, and T. Varghese, "Elastography: Ultrasonic estimation and imaging of the elastic properties of tissues," *Proceedings of the Institution of Mechanical Engineers, Part H: Journal of Engineering in Medicine*, vol. 213, no. 3, pp. 203–233, 1999.

[13] A. Chaudhry, *Effect of Boundary Conditions on Performance of Poroelastographic Imaging Techniques in Non Homogenous Poroelastic Media*. Thesis, 2010.

[14] B. A. Galaz and R. H. Acevedo, "Optimization of a pixel-to-pixel curve-fitting method for poroelastography imaging," *Ultrasound in Medicine and Biology*, vol. 43, no. 1, pp. 309–322, 2017.

[15] P. R. Perriñez, A. J. Pattison, F. E. Kennedy, J. B. Weaver, and K. D. Paulsen, "Contrast detection in fluid-saturated media with magnetic resonance poroelastography," *Medical Physics*, vol. 37, no. 7Part1, pp. 3518–3526, 2010.

[16] M. T. Islam, E. Tasciotti, and R. Righetti, "Estimation of vascular permeability in irregularly shaped cancers using ultrasound poroelastography," *IEEE Transactions on Biomedical Engineering*, vol. 67, no. 4, pp. 1083–1096, 2020.

[17] M. T. Islam, A. Chaudhry, S. Tang, E. Tasciotti, and R. Righetti, "A new method for estimating the effective poisson's ratio in ultrasound poroelastography," *IEEE Transactions on Medical Imaging*, vol. 37, no. 5, pp. 1178–1191, 2018.

[18] R. Righetti, J. Ophir, B. S. Garra, R. M. Chandrasekhar, and T. A. Krouskop, "A new method for generating poroelastograms in noisy environments," *Ultrasonic Imaging*, vol. 27, no. 4,

pp. 201–220, 2005.

[19] V. Michaud, *Permeability properties of composite reinforcements*, pp. 443–472. Woodhead Publishing, 2021.

[20] P. A. Netti, L. T. Baxter, Y. Boucher, R. Skalak, and R. K. Jain, “Macro- and microscopic fluid transport in living tissues: Application to solid tumors,” *AIChE Journal*, vol. 43, no. 3, pp. 818–834, 1997.

[21] H. Maeda, J. Wu, T. Sawa, Y. Matsumura, and K. Hori, “Tumor vascular permeability and the epr effect in macromolecular therapeutics: a review,” *Journal of Controlled Release*, vol. 65, no. 1-2, pp. 271–284, 2000.

[22] D. R. Senger, S. J. Galli, A. M. Dvorak, C. A. Perruzzi, V. S. Harvey, and H. F. Dvorak, “Tumor cells secrete a vascular permeability factor that promotes accumulation of ascites fluid,” *Science*, vol. 219, no. 4587, pp. 983–985, 1983.

[23] H. T. Nia, L. L. Munn, and R. K. Jain, “Physical traits of cancer,” *Science*, vol. 370, no. 6516, p. eaaz0868, 2020.

[24] E. Detournay and A. H. D. Cheng, *Fundamentals of Poroelasticity*, pp. 113–171. Oxford: Pergamon, 1993.

[25] T. Stylianopoulos, J. D. Martin, V. P. Chauhan, S. R. Jain, B. Diop-Frimpong, N. Bardeesy, B. L. Smith, C. R. Ferrone, F. J. Hornicek, Y. Boucher, L. L. Munn, and R. K. Jain, “Causes, consequences, and remedies for growth-induced solid stress in murine and human tumors,” *Proceedings of the National Academy of Sciences*, vol. 109, no. 38, pp. 15101–15108, 2012.

[26] Vikash, Y. Boucher, Cristina, S. Roberge, John, T. Stylianopoulos, N. Bardeesy, Ronald, Timothy, Lance, and Rakesh, “Compression of pancreatic tumor blood vessels by hyaluronan is caused by solid stress and not interstitial fluid pressure,” *Cancer Cell*, vol. 26, no. 1, pp. 14–15, 2014.

[27] H. Wiig and M. A. Swartz, “Interstitial fluid and lymph formation and transport: Physiological regulation and roles in inflammation and cancer,” *Physiological Reviews*, vol. 92, no. 3, pp. 1005–1060, 2012.

[28] T. Stylianopoulos, J. D. Martin, M. Snuderl, F. Mpekris, S. R. Jain, and R. K. Jain, "Coevolution of solid stress and interstitial fluid pressure in tumors during progression: Implications for vascular collapse," *Cancer Research*, vol. 73, no. 13, pp. 3833–3841, 2013.

[29] J. S. Young, C. E. Llumsden, and A. L. Stalker, "The significance of the "tissue pressure" of normal testicular and of neoplastic (brown-pearce carcinoma) tissue in the rabbit," *The Journal of Pathology and Bacteriology*, vol. 62, no. 3, pp. 313–333, 1950.

[30] Y. Boucher, L. T. Baxter, and R. K. Jain, "Interstitial pressure gradients in tissue-isolated and subcutaneous tumors: implications for therapy," *Cancer Res*, vol. 50, no. 15, pp. 4478–84, 1990.

[31] M. Milosevic, A. Fyles, D. Hedley, M. Pintilie, W. Levin, L. Manchul, and R. Hill, "Interstitial fluid pressure predicts survival in patients with cervix cancer independent of clinical prognostic factors and tumor oxygen measurements," *Cancer Res*, vol. 61, no. 17, pp. 6400–5, 2001.

[32] M. Kalli and T. Stylianopoulos, "Defining the role of solid stress and matrix stiffness in cancer cell proliferation and metastasis," *Frontiers in Oncology*, vol. 8, 2018.

[33] M. W. Dewhirst and T. W. Secomb, "Transport of drugs from blood vessels to tumour tissue," *Nature Reviews Cancer*, vol. 17, no. 12, pp. 738–750, 2017.

[34] M. D. Nieskoski, *Influence of Solid Stress Upon Pancreatic Cancer Therapy*. Ph.d., 2017.

[35] M. T. Islam, J. N. Reddy, and R. Righetti, "A model-based approach to investigate the effect of elevated interstitial fluid pressure on strain elastography," *Physics in Medicine and Biology*, vol. 63, no. 21, p. 215011, 2018.

[36] M. T. Islam and R. Righetti, "A novel finite element model to assess the effect of solid stress inside tumors on elastographic normal strains and fluid pressure," *Journal of Engineering and Science in Medical Diagnostics and Therapy*, vol. 2, no. 3, 2019.

[37] M. T. Islam, S. Tang, C. Liverani, S. Saha, E. Tasciotti, and R. Righetti, "Non-invasive imaging of young's modulus and poisson's ratio in cancers in vivo," *Scientific Reports*, vol. 10, no. 1, 2020.

[38] J. P. Laible, D. Pflaster, B. R. Simon, M. H. Krag, M. Pope, and L. D. Haugh, "A dynamic material parameter estimation procedure for soft tissue using a poroelastic finite element model," *Journal of Biomechanical Engineering*, vol. 116, no. 1, pp. 19–29, 1994.

[39] M. A. Biot, "Mechanics of deformation and acoustic propagation in porous media," *Journal of Applied Physics*, vol. 33, no. 4, pp. 1482–1498, 1962.

[40] J. D. Eshelby, "Elastic inclusions and inhomogeneities,"

[41] J. R. Rice, J. W. RUDNICKIS, and D. A. SIMONS, "Deformation of spherical cavities and inclusions in fluid-infiltrated elastic materials,"

[42] M. T. Islam, A. Chaudhry, G. Unnikrishnan, J. N. Reddy, and R. Righetti, "An analytical poroelastic model for ultrasound elastography imaging of tumors," *Physics in Medicine and Biology*, vol. 63, no. 2, p. 025031, 2018.

[43] M. T. Islam, J. N. Reddy, and R. Righetti, "An analytical poroelastic model of a non-homogeneous medium under creep compression for ultrasound poroelastography applications - part i," *J Biomech Eng*, 2018.

[44] M. T. Islam, J. N. Reddy, and R. Righetti, "An analytical poroelastic model of a non-homogeneous medium under creep compression for ultrasound poroelastography applications - part ii," *J Biomech Eng*, 2018.

[45] L. T. Baxter and R. K. Jain, "Transport of fluid and macromolecules in tumors. i. role of interstitial pressure and convection," *Microvascular Research*, vol. 37, no. 1, pp. 77–104, 1989.

[46] R. Leiderman, P. E. Barbone, A. A. Oberai, and J. C. Bamber, "Coupling between elastic strain and interstitial fluid flow: ramifications for poroelastic imaging," *Physics in Medicine and Biology*, vol. 51, no. 24, pp. 6291–6313, 2006.

[47] M. Omidyeganeh, Y. Xiao, M. O. Ahmad, and H. Rivaz, "Estimation of strain elastography from ultrasound radio-frequency data by utilizing analytic gradient of the similarity metric," *IEEE Transactions on Medical Imaging*, vol. 36, no. 6, pp. 1347–1358, 2017.

[48] H. Rivaz, E. Boctor, P. Foroughi, R. Zellars, G. Fichtinger, and G. Hager, "Ultrasound

elastography: A dynamic programming approach," *IEEE Transactions on Medical Imaging*, vol. 27, no. 10, pp. 1373–1377, 2008.

[49] R. G. P. Lopata, M. M. Nillesen, H. H. G. Hansen, I. H. Gerrits, J. M. Thijssen, and C. L. de Korte, "Performance of two dimensional displacement and strain estimation techniques using a phased array transducer," *Ultrasound in Medicine and Biology*, vol. 35, no. 12, pp. 2031–2041, 2009.

[50] M. Hussain, E. Abu Anas, S. Alam, S. Lee, and M. Hasan, "Direct and gradient-based average strain estimation by using weighted nearest neighbor cross-correlation peaks," *IEEE Transactions on Ultrasonics, Ferroelectrics and Frequency Control*, vol. 59, no. 8, pp. 1713–1728, 2012.

[51] M. Omidyeganeh, Y. Xiao, M. O. Ahmad, and H. Rivaz, "Estimation of strain elastography from ultrasound radio-frequency data by utilizing analytic gradient of the similarity metric," *IEEE Transactions on Medical Imaging*, vol. 36, no. 6, pp. 1347–1358, 2017.

[52] M. Ke, J. Chen, and H. Jin, "Research of using dynamic programming in the nodes encoding optimization," IEEE.

[53] X. Gong and S. Bansmer, "Horn–schunck optical flow applied to deformation measurement of a birdlike airfoil," *Chinese Journal of Aeronautics*, vol. 28, no. 5, pp. 1305–1315, 2015.

[54] A. Thitaikumar and J. Ophir, "Effect of lesion boundary conditions on axial strain elastograms: A parametric study," *Ultrasound in Medicine and Biology*, vol. 33, no. 9, pp. 1463–1467, 2007.

[55] J. Ophir, I. Céspedes, H. Ponnekanti, Y. Yazdi, and X. Li, "Elastography: A quantitative method for imaging the elasticity of biological tissues," *Ultrasonic Imaging*, vol. 13, no. 2, pp. 111–134, 1991.

[56] M. O'Donnell, A. R. Skovoroda, B. M. Shapo, and S. Y. Emelianov, "Internal displacement and strain imaging using ultrasonic speckle tracking," *IEEE Transactions on Ultrasonics, Ferroelectrics and Frequency Control*, vol. 41, no. 3, pp. 314–325, 1994.

[57] A. A. H. Sayed, *Novel 3D Ultrasound Elastography Techniques for In Vivo Breast Tumor*

Imaging and Nonlinear Characterization. Thesis, 2013.

[58] H. Chen and T. Varghese, "Principal component analysis of shear strain effects," *Ultrasonics*, vol. 49, no. 4-5, pp. 472–483, 2009.

[59] A. Thitaikumar, T. A. Krouskop, B. S. Garra, and J. Ophir, "Visualization of bonding at an inclusion boundary using axial-shear strain elastography: a feasibility study," *Phys Med Biol*, vol. 52, no. 9, pp. 2615–33, 2007.

[60] T. A. Krouskop, T. M. Wheeler, F. Kallel, B. S. Garra, and T. Hall, "Elastic moduli of breast and prostate tissues under compression," *Ultrasonic Imaging*, vol. 20, no. 4, pp. 260–274, 1998.

[61] C. Schmitt, G. Soulez, R. L. Maurice, M.-F. Giroux, and G. Cloutier, "Noninvasive vascular elastography: Toward a complementary characterization tool of atherosclerosis in carotid arteries," *Ultrasound in Medicine and Biology*, vol. 33, no. 12, pp. 1841–1858, 2007.

[62] E. Konofagou and J. Ophir, "A new elastographic method for estimation and imaging of lateral displacements, lateral strains, corrected axial strains and poisson's ratios in tissues," *Ultrasound in Medicine and Biology*, vol. 24, no. 8, pp. 1183–1199, 1998.

[63] A. R. Skovoroda, M. A. Lubinski, S. Y. Emelianov, and M. O'Donnell, "Nonlinear estimation of the lateral displacement using tissue incompressibility," *IEEE Transactions on Ultrasonics, Ferroelectrics and Frequency Control*, vol. 45, no. 2, pp. 491–503, 1998.

[64] U. Techavipoo, Q. Chen, T. Varghese, and J. A. Zagzebski, "Estimation of displacement vectors and strain tensors in elastography using angular insonifications," *IEEE Transactions on Medical Imaging*, vol. 23, no. 12, pp. 1479–1489, 2004.

[65] E. E. Konofagou, T. Harrigan, and J. Ophir, "Shear strain estimation and lesion mobility assessment in elastography," *Ultrasonics*, vol. 38, no. 1-8, pp. 400–404, 2000.

[66] H. Xu, M. Rao, T. Varghese, A. Sommer, S. Baker, T. J. Hall, G. A. Sisney, and E. S. Burnside, "Axial-shear strain imaging for differentiating benign and malignant breast masses," *Ultrasound in Medicine and Biology*, vol. 36, no. 11, pp. 1813–1824, 2010.

[67] A. K. Thittai, J.-M. Yamal, L. M. Mobbs, C. M. Kraemer-Chant, S. Chekuri, B. S. Garra,

and J. Ophir, “Axial-shear strain elastography for breast lesion classification: Further results from in vivo data,” *Ultrasound in Medicine and Biology*, vol. 37, no. 2, pp. 189–197, 2011.

[68] F. Viola and W. F. Walker, “Shear strain elastography,” IEEE.

[69] M. Rao, Q. Chen, H. Shi, T. Varghese, E. L. Madsen, J. A. Zagzebski, and T. A. Wilson, “Normal and shear strain estimation using beam steering on linear-array transducers,” *Ultrasound in Medicine and Biology*, vol. 33, no. 1, pp. 57–66, 2007.

[70] R. L. Maurice, J. Ohayon, Y. Fretigny, M. Bertrand, G. Soulez, and G. Cloutier, “Non-invasive vascular elastography: Theoretical framework,” *IEEE Transactions on Medical Imaging*, vol. 23, no. 2, pp. 164–180, 2004.

[71] R. v. Mises, “Mechanics of solid bodies in the plastically-deformable state,”

[72] H. Zhang, M. Song, M. Yang, Y. Song, F. Zhang, A. Zhang, L. Ruan, and M. Wan, “Fast von mises strain imaging on ultrasound carotid vessel wall by flow driven diffusion method,” *Australasian Physical & Engineering Sciences in Medicine*, vol. 41, no. 3, pp. 669–686, 2018.

[73] I. K. Zervantonakis, S. D. Fung-Kee-Fung, W. N. Lee, and E. E. Konofagou, “A novel, view-independent method for strain mapping in myocardial elastography: eliminating angle and centroid dependence,” *Physics in Medicine and Biology*, vol. 52, no. 14, pp. 4063–4080, 2007.

[74] C. Jia, R. Olafsson, K. Kim, T. J. Kolias, J. M. Rubin, W. F. Weitzel, R. S. Witte, S.-W. Huang, M. S. Richards, C. X. Deng, and M. O’Donnell, “Two-dimensional strain imaging of controlled rabbit hearts,” *Ultrasound in Medicine and Biology*, vol. 35, no. 9, pp. 1488–1501, 2009.

[75] R. Nayak, S. Huntzicker, J. Ohayon, N. Carson, V. Dogra, G. Schifitto, and M. M. Doyley, “Principal strain vascular elastography: Simulation and preliminary clinical evaluation,” *Ultrasound in Medicine and Biology*, vol. 43, no. 3, pp. 682–699, 2017.

[76] H. Li, B. Chayer, M.-H. Roy Cardinal, J. Muijsers, M. Van Den Hoven, Z. Qin, M. Gesnik, G. Soulez, R. G. P. Lopata, and G. Cloutier, “Investigation of out-of-plane motion artifacts in

2d noninvasive vascular ultrasound elastography," *Physics in Medicine and Biology*, vol. 63, no. 24, p. 245003, 2018.

[77] R. G. Barr and A. E. Lackey, "The utility of the "bull's-eye" artifact on breast elasticity imaging in reducing breast lesion biopsy rate," *Ultrasound Quarterly*, vol. 27, no. 3, 2011.

[78] C. Dietrich, R. Barr, A. Farrokh, M. Dighe, M. Hocke, C. Jenssen, Y. Dong, A. Saftoiu, and R. Havre, "Strain elastography - how to do it?," *Ultrasound International Open*, vol. 03, no. 04, pp. E137–E149, 2017.

[79] H. Zhi, B. Ou, B.-M. Luo, X. Feng, Y.-L. Wen, and H.-Y. Yang, "Comparison of ultrasound elastography, mammography, and sonography in the diagnosis of solid breast lesions," *Journal of Ultrasound in Medicine*, vol. 26, no. 6, pp. 807–815, 2007.

[80] P. Rzymski and T. Opala, "Elastography as a new diagnostic tool to detect breast cancer – evaluation of research and clinical applications," *Przegląd Menopauzalny*, vol. 5: 357–362, 2011.

[81] Y.-C. Fung, *Mechanical Properties and Active Remodeling of Blood Vessels*, pp. 321–391. Springer New York, 1993.

[82] F. Mpekris, J. W. Baish, T. Stylianopoulos, and R. K. Jain, "Role of vascular normalization in benefit from metronomic chemotherapy," *Proceedings of the National Academy of Sciences*, vol. 114, no. 8, pp. 1994–1999, 2017.

[83] T. Stylianopoulos, J. D. Martin, M. Snuderl, F. Mpekris, S. R. Jain, and R. K. Jain, "Coevolution of solid stress and interstitial fluid pressure in tumors during progression: Implications for vascular collapse," *Cancer Research*, vol. 73, no. 13, pp. 3833–3841, 2013.

[84] J. R. Less, M. C. Posner, Y. Boucher, D. Borochovitz, N. Wolmark, and R. K. Jain, "Interstitial hypertension in human breast and colorectal tumors," *Cancer Res*, vol. 52, no. 22, pp. 6371–4, 1992.

[85] M. F. Milosevic, A. W. Fyles, R. Wong, M. Pintilie, M.-C. Kavanagh, W. Levin, L. A. Manchul, T. J. Keane, and R. P. Hill, "Interstitial fluid pressure in cervical carcinoma," *Cancer*, vol. 82, no. 12, pp. 2418–2426, 1998.

[86] H. T. Nia, H. Liu, G. Seano, M. Datta, D. Jones, N. Rahbari, J. Incio, V. P. Chauhan, K. Jung, J. D. Martin, V. Askoxylakis, T. P. Padera, D. Fukumura, Y. Boucher, F. J. Hornicek, A. J. Grodzinsky, J. W. Baish, L. L. Munn, and R. K. Jain, "Solid stress and elastic energy as measures of tumour mechanopathology," *Nature Biomedical Engineering*, vol. 1, no. 1, p. 0004, 2017.

[87] S. Celi, F. Di Puccio, and P. Forte, "Advances in finite element simulations of elastosonography for breast lesion detection," *Journal of Biomechanical Engineering*, vol. 133, no. 8, p. 081006, 2011.

[88] V. Narang, S. Y. Wong, S. R. Leong, B. Harish, J.-P. Abastado, and A. Gouaillard, "Selection of mesenchymal-like metastatic cells in primary tumors - an in silico investigation," *Frontiers in immunology*, vol. 3, pp. 88–88, 2012.

[89] M. F. Coughlin, D. R. Bielenberg, G. Lenormand, M. Marinkovic, C. G. Waghorne, B. R. Zetter, and J. J. Fredberg, "Cytoskeletal stiffness, friction, and fluidity of cancer cell lines with different metastatic potential," *Clinical & Experimental Metastasis*, vol. 30, no. 3, pp. 237–250, 2013.

[90] J. Jiang and B. Peng, "A normalized shear deformation indicator for ultrasound strain elastography in breast tissues: An in vivo feasibility study," *BioMed Research International*, vol. 2018, pp. 1–11, 2018.

[91] M. Sarntinoranont, F. Rooney, and M. Ferrari, "Interstitial stress and fluid pressure within a growing tumor," *Annals of Biomedical Engineering*, vol. 31, no. 3, pp. 327–335, 2003.

[92] J. O. Waldeland, J.-V. Gaustad, E. K. Rofstad, and S. Evje, "In silico investigations of intratumoral heterogeneous interstitial fluid pressure," *Journal of Theoretical Biology*, vol. 526, p. 110787, 2021.

[93] Abaqus, *ABAQUS/Standard User's Manual, Version 6.14*. Dassault Systemes Simulia Corp, 2014.

[94] K. v. Terzaghi, "The shearing resistance of saturated soils and the angle between the planes of shear," in *First international conference on soil Mechanics, 1936*, vol. 1, pp. 54–59.

[95] G. P. Berry, J. C. Bamber, C. G. Armstrong, N. R. Miller, and P. E. Barbone, "Towards an acoustic model-based poroelastic imaging method: I. theoretical foundation," *Ultrasound in Medicine and Biology*, vol. 32, no. 4, pp. 547–567, 2006.

[96] J. Barlow, "Optimal stress locations in finite element models," *International Journal for Numerical Methods in Engineering*, vol. 10, no. 2, pp. 243–251, 1976.

[97] T. Varghese and J. Ophir, "Estimating tissue strain from signal decorrelation using the correlation coefficient," *Ultrasound in Medicine and Biology*, vol. 22, no. 9, pp. 1249–1254, 1996.

[98] R. R. Desai, T. A. Krouskop, and R. Righetti, "Elastography using harmonic ultrasonic imaging: A feasibility study," *Ultrasonic Imaging*, vol. 32, no. 2, pp. 103–117, 2010.

[99] R. Righetti, J. Ophir, S. Srinivasan, and T. A. Krouskop, "The feasibility of using elastography for imaging the poisson's ratio in porous media," *Ultrasound in Medicine and Biology*, vol. 30, no. 2, pp. 215–228, 2004.

[100] C. Pan, O. Schoppe, A. Parra-Damas, R. Cai, M. I. Todorov, G. Gondi, B. V. Neubeck, A. Ghasemi, M. A. Reimer, J. Coronel, B. K. Garvalov, B. Menze, R. Zeidler, and A. Ertürk, "Deep learning reveals cancer metastasis and therapeutic antibody targeting in whole body." 2019.

[101] T. R. Kumm and M. M. Szabunio, "Elastography for the characterization of breast lesions: Initial clinical experience," *Cancer Control*, vol. 17, no. 3, pp. 156–161, 2010.

[102] R. G. Barr, "Real-time ultrasound elasticity of the breast: initial clinical results," *Ultrasound Q*, vol. 26, no. 2, pp. 61–6, 2010.